POLITECNICO
MILANO 1863

Spacecraft Structural Compliance Analysis to Ariane-VI
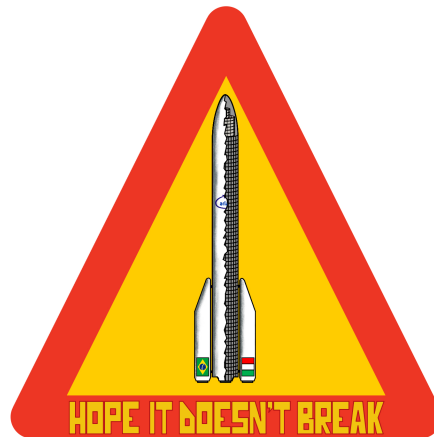
Name	Student ID	Email
Aloscari Davide	10658793	davide.aloscari@mail.polimi.it
Cappellacci Tommaso	10704229	tommaso.cappellacci@mail.polimi.it
Lima Augusto	10916450	augustojose.silvestredelima@mail.polimi.it
Malatesta Kail	10697364	kail.malatesta@mail.polimi.com
Torre Federico	10645141	federico.torre@mail.polimi.it
Zara Andrea	10698650	andrea.zara@mail.polimi.it

Course of Analysis and Testing of Space Structures
School of Industrial Engineering
Academic Year 2023-2024
Prof. Pietro Nali

Abstract

The following work was developed as part of the "Analysis and Testing of Space Structures" course aiming to perform a complete structural analysis of a Spacecraft so as to check its compliance with the Launch Vehicle Ariane VI's launch requirements. Hence, using tools such Finite Element Models of the Launch Vehicle and the Spacecraft, *Matlab* codes and *Excel* spreadsheets, the project contains all required analysis to be performed throughout the design process and theoretical verification of a satellite's structures.

Acronyms

APSD Acceleration Power Spectral Density

CoG Center of gravity

CTE Coefficient of Thermal Expansion

CAD Computer aided design

CLA Coupled Load Analysis

DOF Degrees of freedom

ERS Extreme Response Spectrum

ESI Equivalent Sine Input

ECSS European Cooperation for Space Standardization

F-F Free-Free

FE Finite element

FEM Finite element model

FOS Factor of safety

gRMS Root Mean Square acceleration

HM Hard-Mounted

IF Interface

IUT Item Under Test

LV Launch vehicle

MDOF Multiple Degree of Freedom

MLI Multi Layer Insulation

MoS Margin of Safety

OASPL OverAll Sound Pressure Level

$\mathbf{P}_{RMS}$ Pressure Root Mean Square

$\mathbf{P}_{ref}$ Pressure reference

PPSD Pressure Power Spectral Density

QSL Quasi static load

RIF Ring interface diameter

SC Spacecraft

SF Seafty factor

SRS Shock Response Spectrum

SPL Sound Pressure Levels

UM User manual

Contents

List of Figures

List of Tables

Chapter 1

Introduction

The present work was developed as part of the "Analysis and Testing of Space Structures" aiming to perform a complete structural analysis of a Spacecraft so as to check its compliance with the Launch Vehicle Ariane 6's launch requirements according to its User's Manual [1] and other additional mission related requirements. Hence, a set of analysis are performed in order to guarantee that the Spacecraft and its Payload will survive the launch and space environments, as well as that it will provide enough structural stability and strength for the mission to be successful.

The following analysis were considered in this project:

- Modal Analysis

- Static Analysis

- Dynamic Coupling Analysis

- Thermoelastic Analysis

- Sine Test Prediction Analysis

- Acoutic Vibration Analysis

- Severity Analysis

- Buckling Analysis

For such, tools like Finite Element Models (created using Femap and solved via MSC Nastran), *Matlab* codes and *Excel* spreadsheets were used. Finally, after the presentation of all results, a final compliance check is performed.

Chapter 2

LV and SC modeling

2.1   Ariane 6

Ariane 6 is an European expendable launch system developed by ArianeGroup on behalf of the ESA (European Space Agency) since the early 2010s. It succeeds the Ariane 5 within the Ariane launch vehicle family. The primary goals of Ariane 6 are to reduce launch costs by half compared to Ariane 5 and to increase the annual launch capacity from six or seven to up to eleven missions. Ariane 6 consists of three stages: two or four strap-on boosters and a central core composed of lower and upper stages. The lower stage, equipped with solid rocket boosters, initiates the launch with 135 tonnes of thrust in vacuum. The core stage is powered by the upgraded liquid-fuelled Vulcain 2.1 engine, derived from Ariane 5's Vulcain 2 engine, and two or four P120C boosters that provide additional thrust during liftoff. The upper stage utilizes the reignitable Vinci engine, fueled by cryogenic liquid oxygen and hydrogen, enabling Ariane 6 to access a variety of orbits within a single mission and accommodate multiple payloads. The upper stage undergoes one, two, or more burns as necessary to achieve the desired orbits. Following payload separation, a final burn is conducted to deorbit the upper stage and mitigate space debris.
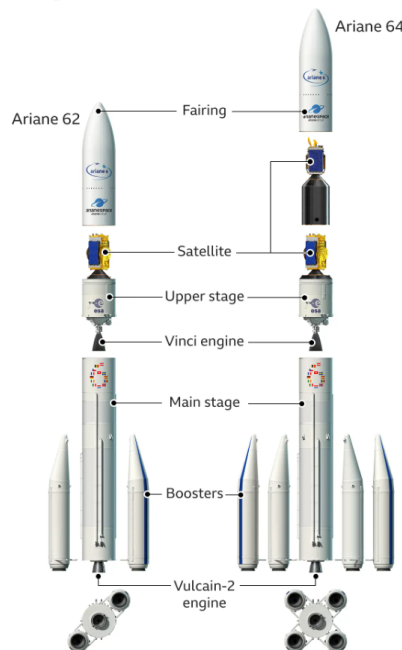
Figure 2.1: Flight envelope.

Between the two versions in Fig 2.1, the Ariane 62 design - the one with two boosters - has been selected for this project.

The off-the-shelf adapter chosen is the PAF 1666 model, with the properties found in Table 2.1, from LV User manual (UM).

Diameter	Height	Mass
1666 mm	450 mm	70 kg

Table 2.1: PAF 1666 adapter properties.

Both launcher and adapter have been modeled on Femap at 1:1 scale. The overall geometry has been shaped such that it is consistent with that of the real launcher, considering only the external structure and not any internal components. The FEM model of the launcher - along with the two propulsion boosters - is shown in Figure 2.2, and consists in 7209 linear plate elements.
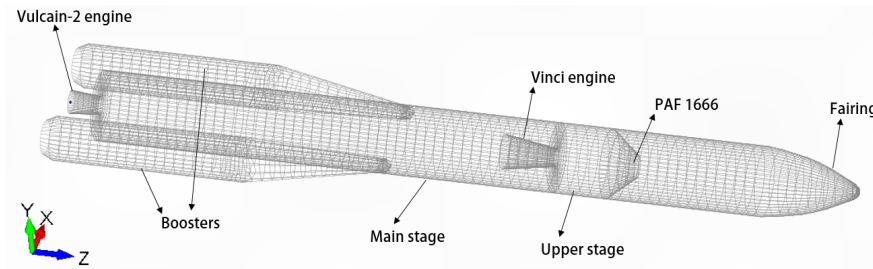
Figure 2.2: Model of the launcher.

2.2 Spacecraft

The SC has been modeled as an axial-symmetrical body, with a FEM mesh of 1882 linear plate elements. It includes one concentrated mass of 100 kg representing the telescope on the top plate and two concentrated masses of 10 kg representing two star tracker units. These masses are placed in opposite positions with respect to the central axis of symmetry, as illustrated in Figure 2.3.
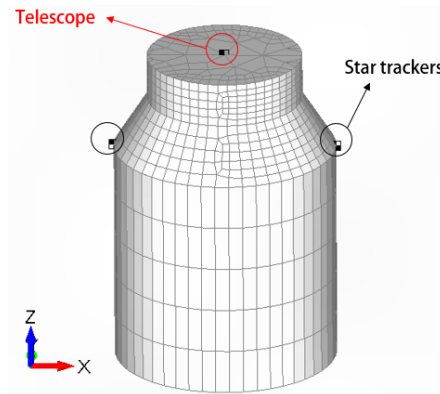
Figure 2.3: Model of the spacecraft.

2.3   Fairing dimensions

The fairing serves a crucial role in shielding satellites from the thermal, acoustic, and aerodynamic forces encountered during their journey into space. In the case of Ariane 6, a distinctive ogive-shaped fairing is employed at the apex, offering two variants: one measuring 18 meters (A64/A62) and the other 14 meters (A62) in length.For the present undertaking, the fairing design with a 18-meter height has been designated. Following this determination, it is imperative to ensure that the satellite's dimensions are compatible with those of the fairing. Figure 2.4 illustrates the Computer aided design (CAD) rendering, presenting the potential usable volume of the configuration utilized for the model used throughout this project. The model is a simplification of the real one accordingly with the goal of this analysis.
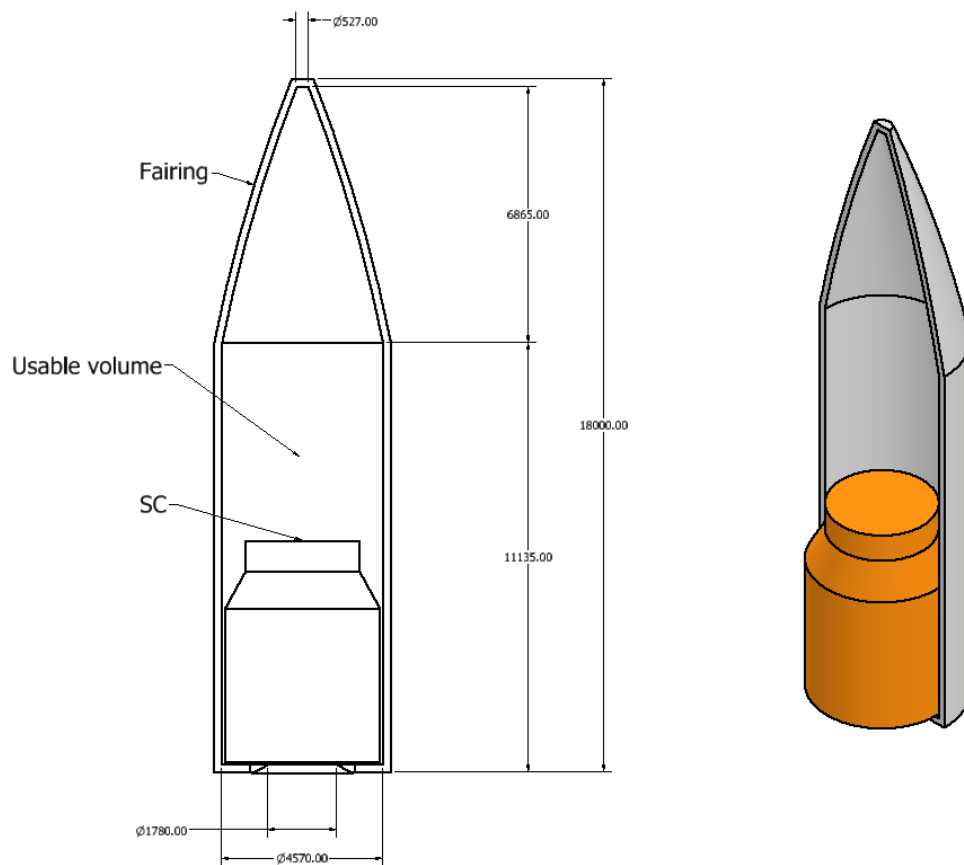
Figure 2.4: Usable volume.

Chapter 3

Modal analysis

The modal analysis is crucial to prevent the occurrence of unwanted harmonic resonances during launch, which could lead to catastrophic consequences. If the dynamic interaction between the structures of the LV and SC are completely detached, their design processes can be conducted independently. To adjust the frequencies of both the LV and SC, the following methodology has been employed:

1. Initially, the frequencies of the LV are calculated using an MSC Nastran Free-Free (F-F) modal analysis, focusing solely on the isolated LV model. This analysis utilizes the 103 solution sequence code for Modal analysis.

2. Subsequently, the frequencies of the SC are determined through a Hard-Mounted (HM) modal analysis, wherein the interface nodes on the SC ring are fixed across all six degrees of freedom DOFs.

3. Finally, a comprehensive F-F analysis is performed, considering the launcher and spacecraft interconnected through the interface. Given the spacecraft's significantly lower mass compared to the launcher, minimal variations are expected in the LV frequencies. Consistency in the SC frequencies with the previous scenario validates the results.

3.1   Launcher frequency requirements

The thresholds mentioned in the introduction of Chapter 3 are presented in Table 3.1 and are sourced from the UM [1].

	Requirement	Description
Lat. Frequency [Hz]	≥ 6	The fundamental (primary) frequency in the lateral axis of a Spacecraft cantilevered.
Long. Frequncy [Hz]	≥ 20	The fundamental (primary) frequency in the longitudinal axis of a SC cantilevered at the interface.

Table 3.1: Requirements on primary mode.

3.2   Launcher parameters

Starting from the criteria set by the launcher authority [1], adjustments can be made to the material and plate characteristics of the LV to ensure that the simulated launcher is representative of the actual one. This process involves employing a trial-and-error methodology to concurrently fine-tune the physical attributes of the model along with its frequencies. The selection of parameters is guided by the objective of achieving frequencies that meet the specified thresholds outlined in Table 3.1. Should be noted that the presented properties are not representative of a specific material on the market, but this choice can be detailed in further analysis of the model.

E [Pa]	G [Pa]	ν [-]	ρ [kg/m^3]
1.8×10^{10}	2.8×10^{10}	0.33	2700

Thickness [m]	Bending stiffness factor
0.1	2000

(a) Materials properties   (b) Plate Properties

Table 3.2: Launch vehicle model.

In Table 3.2 are listed the characteristics of both launcher body and also of the booster that gives a supplement of ΔV during the ascent phase of the mission.

E [Pa]	G [Pa]	ν [-]	ρ [kg/m^3]
1.8×10^{10}	2.8×10^{10}	0.33	4700

Thickness [m]	Bending stiffness factor
0.1	20000

(a) Materials properties   (b) Plate Properties

Table 3.3: Booster model.

Mass [tons]	Lat. frequency [Hz]	Long. frequency [Hz]
529.9	4.039	17.64

Table 3.4: Results of LV tuning process.

As defined in the introduction 3 a criterion that needs to be satisfied is that LV and SC frequencies are detached. In Table 3.4, it is evident that the frequencies obtained differ from those specified for the spacecraft SC.

(a) Lateral mode $f = 4.03$ [Hz]   (b) Lateral mode $f = 4.03$ [Hz]   (c) Longitudinal mode $f = 17.64$ [Hz]
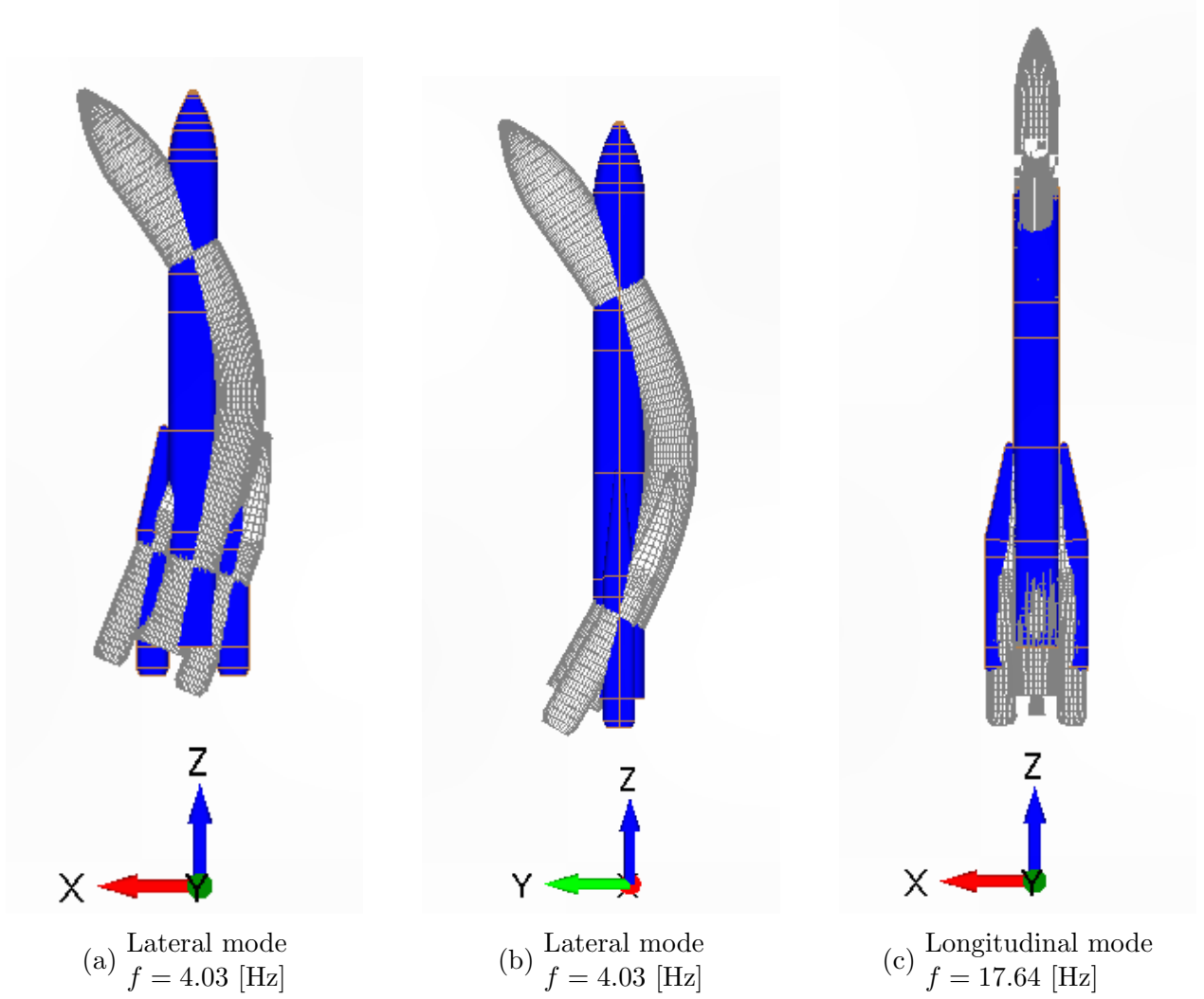
Figure 3.1: Primary modes of the LV with deformation factor 10.

3.3 Spacecraft parameters

The material composition and plate properties of the SC are tuned to align with the specifications outlined in 3.1. Within the SC model, three concentrated masses are incorporated into the axially symmetric structure: one on top to simulate a telescope, and the other two symmetrically positioned relative to the central axis, serving as placeholders for generic units, such as a star tracker. Additionally, a specific constraint is applied to the telescope's mass: to mitigate dynamic coupling effects between the moderately heavy payload and the spacecraft, the top plate of the SC is characterized by distinct properties compared to the remaining body plates as shown in Table 3.5 in particular higher bending stiffness value is used. This differentiation allows for more precise adjustment of the telescope's frequency. The refined material parameters for the SC can be found in Table 3.6 and Table 3.5.

E [Pa]	G [Pa]	ν [-]	ρ [kg/m^3]
1.8×10^{10}	2.8×10^{10}	0.33	2700

(a) Materials properties

Thickness [m]	Bending stiffness factor
0.02	100

(b) Plate Properties

Table 3.5: Top plate SC model.

In Figure 3.2 and 3.3 are depicted the primary modes of both SC and telescope.

E [Pa]	G [Pa]	ν [-]	$\rho \, [kg/m^3]$
1.8×10^{10}	2.8×10^{10}	0.33	2700

(a) Materials properties

Thickness [m]	Bending stiffness factor
0.02	500

(b) Plate Properties

Table 3.6: Body SC model.

Mass [Kg]	Lat. frequency [Hz]	Long. frequency [Hz]
6617.917	13.01	32.95

Table 3.7: Results of SC tuning process.

(a) Lateral mode $f = 13.01$ [Hz]

(b) Lateral mode $f = 13.01$ [Hz]

(c) Longitudinal mode $f = 32.95$ [Hz]
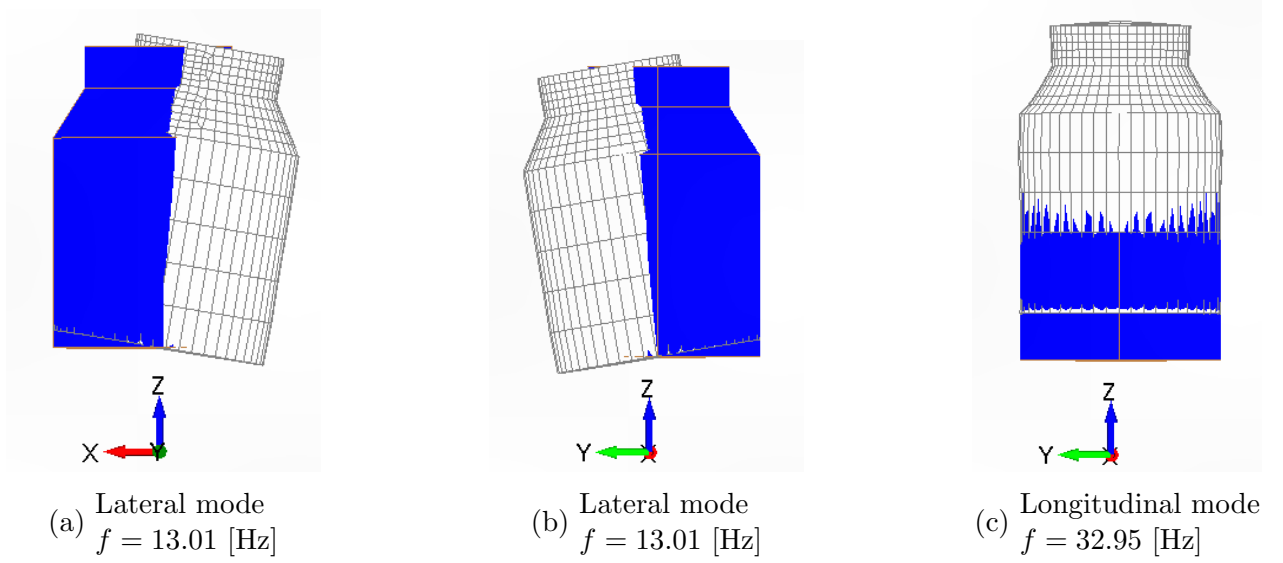
Figure 3.2: Primary modes of the SC with deformation factor 1.
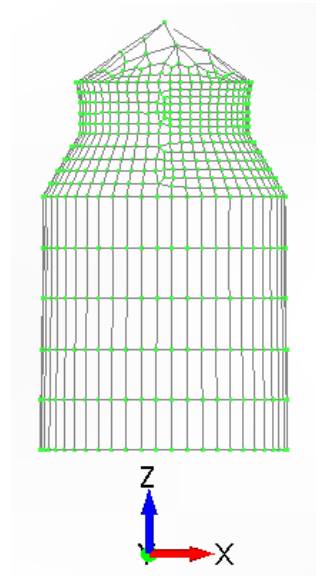
Figure 3.3: Telescope main longitudinal mode.
$f = 26.56[Hz]$

As detailed in 3, a conclusive F-F modal analysis is performed, incorporating the interface connection between the LV and SC.

As depicted in Table 3.8, the frequencies of the launcher remain largely unchanged due to

Scenarios	Lat. frequency [Hz]	Long. frequency[Hz]
F-F launcher	4.039	17.643
Coupled F-F	4.034	17.4255

Table 3.8: Consistency check on LV frequencies.

Scenarios	Lat. frequency [Hz]	Long. frequency[Hz]
HM SC	13.01	32.95
F-F	10.77	30.21

Table 3.9: Consistency check on SC frequencies.

its significantly larger mass compared to the spacecraft SC. While in Table 3.9 the frequencies of the SC experience a slight decrease, this outcome aligns with expectations as the removal of constraints at the interface leads to increased flexibility effects, thereby marginally reducing the overall stiffness of the SC.

3.4   Mass and CoG requirements

Once the tuning of material and plate proper-
ties is complete, it is possible to retrieve from
the FEM the total mass of the spacecraft and
the position of its CoG. These results are dis-
played in Table 3.10 while in Figure 3.4 it
is checked their compliance with the require-
ments coming from the [1].

SC Mass [kg]	z_{CoG} [m]
6617.917	2.723

Table 3.10: Mass and CoG of SC.
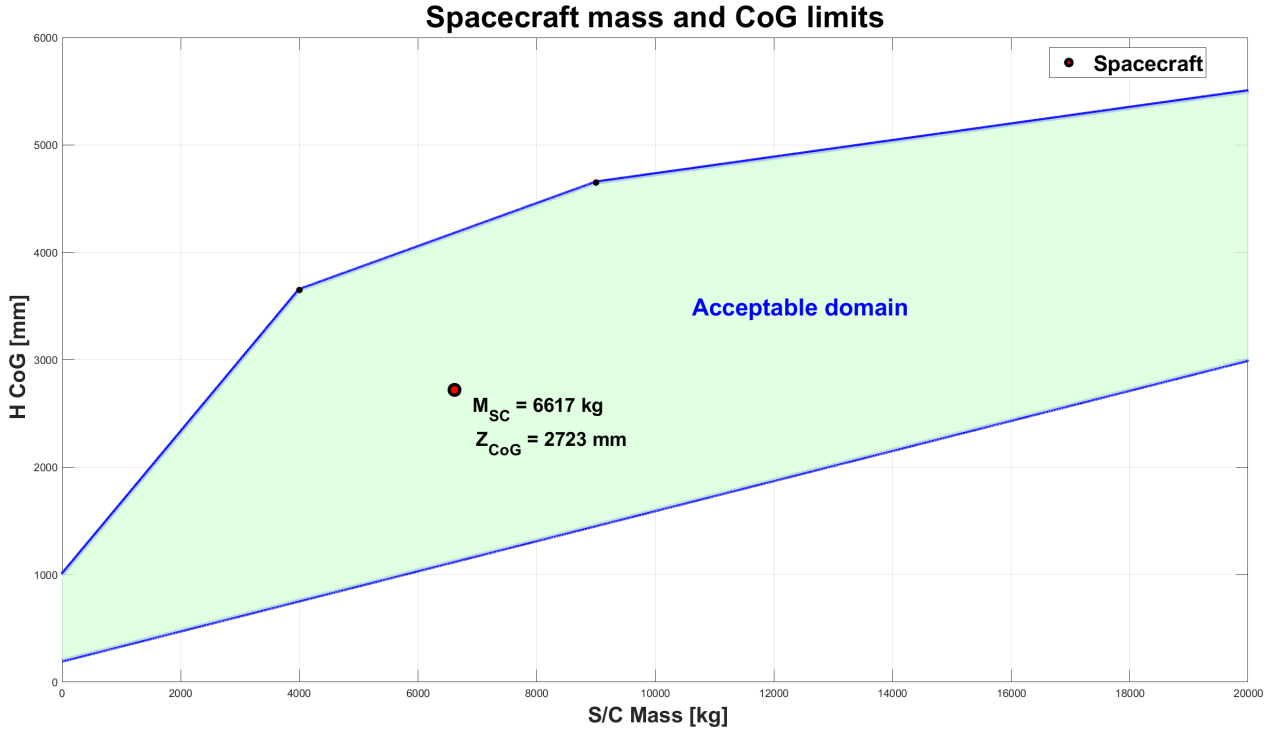
Figure 3.4: Mass and CoG limitations coming from [1].

Chapter 4

Static analysis

4.1 Introduction

The goal of a static or quasi-static analysis is to validate the structural integrity of the spacecraft SC, ensuring its ability to withstand the specified loads detailed in the UM without experiencing any damage or degradation. This involves applying combined loads to the structure during relevant phase of the mission. The SC is secured at the interface ring to facilitate static testing using a shaker: the structure is positioned on a vibrating platform to induce excitation and achieve predefined acceleration levels. Additionally, the launcher authority mandates that the interface efforts between the SC and LV, as calculated during the quasi-static loading, remain below the qualification test values. These QSLs, expressed in gravity units, represent equivalent accelerations applied to the spacecraft structure, encompassing the most severe combination of dynamic and static excitation encountered throughout the mission. These excitations manifest as longitudinal interface forces F_N and lateral interface moments M_{Lat}.

4.2 Line loads and overfluxes

A comprehensive depiction of the flight envelope for Ariane 6 is provided in Figure 4.1. This envelope comprises numerous points, each representing a combination of longitudinal and lateral QSLs encountered during various mission phases, as detailed in Table 4.1. Specifically, the points selected for analysis constitute the perimeter of the envelope itself. It is essential to account for a range of static and dynamic conditions when selecting the excitation to apply. The QSLs specified in the LV user manuals, and similar load specifications, should be viewed as 'static accelerations' which emulate forces and moments equivalent to those arising from more complex loadings where dynamics also play a significant role. Leveraging QSLs is advantageous as they facilitate structure verification through 'static equivalent' analysis, thus obviating the need for elaborate and time-consuming dynamic analyses.

Load event	Longitudinal [g]		Lateral [g]
	Compression	Tension	
Lift-Off	-4.375	1.875	±2.25
Aerodynamic phase	-4.5	1	±2.25
Pressure oscillations	-7.5	1.75	±1.25
ESR jettisoning	-5	3.875	±1.125
LLPM	-5.375	1.75	±0.625
ULPM	-5.625	1.75	±0.625

Table 4.1: QSL during the flight.

The points shown in Figure 4.1 represent various combinations of longitudinal and lateral QSL, collectively contributing to the overall shape of the envelope. The points of interest are those along the flight envelope line that represent the worst-case scenario throughout the entire mission.
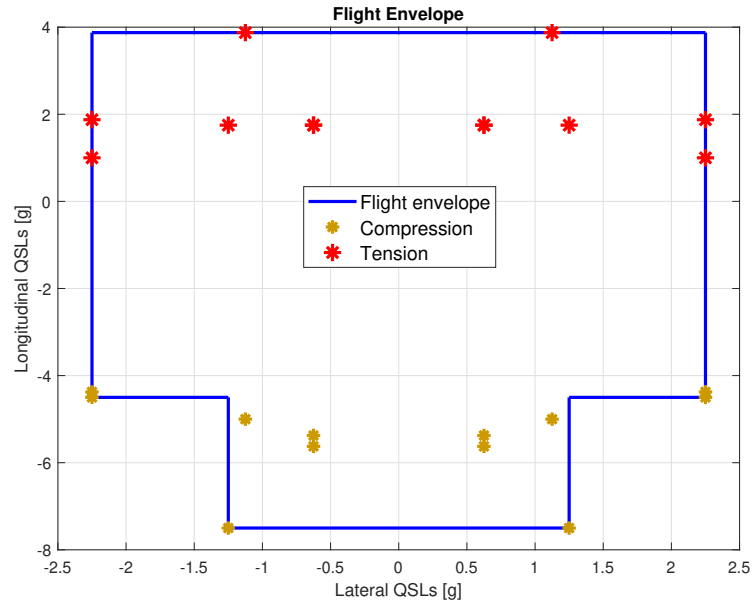
Figure 4.1: Flight envelope.

The chosen adapter is the PAF 1666, resulting in an interface diameter of $D_{\text{IF}} = 1.78$ m (See Figure 4.7. To be complaint with the request of the launch autority the overfluxes must not exceed 10% of off-the-shelf [1]. For every longitudinal and lateral QSL point, the longitudinal interface force F_N and lateral interface moment M_{lat} can be computed as follows:

$$F_N = m_{sc} \cdot \text{QSL}_{\text{Long}} \cdot \text{SF} \tag{4.1}$$

$$M_{\text{lat}} = m_{\text{sc}} \cdot \text{QSL}_{\text{Lat}} \cdot z_{\text{CoG}} \cdot \text{SF} \tag{4.2}$$

In accordance with specifications outlined in the UM [1], the Seafty factor (SF) is defined as 1.25 for qualifications verified through testing. The parameter zCoG represents the longitudinal distance between the center of mass of the spacecraft SC and its base. Additionally, m_{sc} denotes the mass of the spacecraft. Lateral loads are considered along the in-plane axes, namely the x and y directions. Consequently, these loads are evaluated twice: one with My set to zero and M_x equal to M_{Lat}, and the other with M_x set to zero and M_y equal to M_{Lat}. The outcomes in both scenarios are nearly identical due to the quasi-perfect symmetry of the spacecraft SC as shown in Section 4.3. Although the geometry exhibits axial symmetry, small disparities in the mesh lead to a slightly asymmetric distribution of mass and stiffness in the model. The difference between the case in which $M_x = M_{Lat}$ and $M_y = M_{Lat}$ are negligible due to being lower than 0.4% as shown in Table 4.3 . For the sake of completeness, results will be provided for both scenarios. The analytical expression for the line load in case F_N, M_x and M_y are simultaneously present and under the hypothesis of circular ring, denoted as $f_{overall}$ (used for axial-symmetrical structure in which the lateral moments are generated only from the longitudinal line load along the z-axis):

$$f_{\text{overall}} = \frac{F_N}{2\pi RIF} + \frac{M_x}{\pi RIF^2} \cos\left(\theta - \frac{\pi}{4}\right) + \frac{M_y}{\pi RIF^2} \cos\theta \qquad (4.3)$$

Where θ represents the angular coordinate of the interface ring, starting from the x-axis and progressing counterclockwise. The analytical equation provides theoretical flux values for various angles along the circumference of the adapter ring. However, Finite element (FE) computations typically deviate from the analytical predictions due to geometric irregularities and variations in local structural stiffness. These FE computations are designed to closely approximate real-world conditions. Notably, overfluxes would significantly increase for non-symmetric SC designs, as the assumption of ideal overflux computation no longer holds true. Real fluxes are computed from the FE model of the SC using MSC Nastran (101 Static 1g run), where a 1g load is applied along one axis at a time. Figure 4.2 illustrates the deformed structures resulting from these loads.

(a) 1g along x   (b) 1g along y   (c) 1g along z
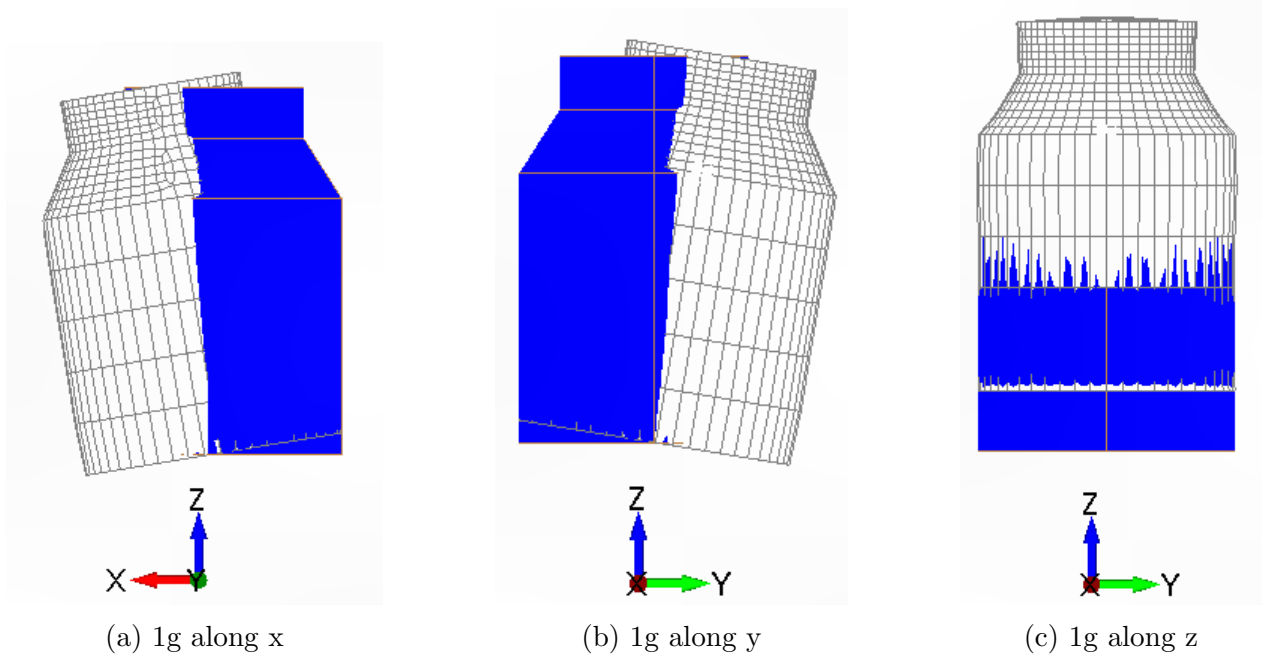
Figure 4.2: Unitary QSL with deformation factor 1.

The overflux factor is then expressed as a percentage for each loading condition:

$$\text{overflux} = \frac{\max|\text{line load curve from FEM}|}{\max|\text{line load calculated analytically}|} \qquad (4.4)$$

A negative value indicates that the absolute value of the real line loads is lower than the theoretically predicted results, and any asymmetries do not result in critical local loading conditions. Conversely, a positive overflux indicates that the real line load exceeds the analytically predicted value, potentially leading to critical conditions, particularly in the tension subcase where the SC could detach from the LV adapter. As previously stated the evaluated load conditions are only those correlated with the extreme QSLs as show in Table 4.3, which are represented by the vertices of the aforementioned flight envelope.

4.3   Results

QSL_{Long} [g]	QSL_{Lat} [g]	Overfluxes [%]	QSL_{Lat} [g]	QSL_{Long} [g]	Overfluxes [%]
-7.5	1.25	-3.946	-7.5	1.25	-3.941
-7.5	-1.25	-3.945	-7.5	-1.25	-3.941
-4.5	2.25	-5.923	-4.5	2.25	-5.920
-4.5	-2.25	-5.923	-4.5	-2.25	-5.920
-4.375	-2.25	-5.964	-4.375	-2.25	-5.961
-4.375	2.25	-5.964	-4.375	2.25	-5.961
1	2.25	<mark>-7.343</mark>	1	2.25	<mark>-7.342</mark>
1	-2.25	<mark>-7.343</mark>	1	-2.25	<mark>-7.342</mark>
1.875	2.25	-6.928	1.875	2.25	-6.927
1.875	-2.25	-6.928	1.875	-2.25	-6.927
3.875	1.125	-5.018	3.875	1.125	-5.014
3.875	-1.125	-5.018	3.875	-1.125	-5.014

(a) $M_y = 0$, $M_x = M_{Lat}$	(b) $M_x = 0$, $M_y = M_{Lat}$

Figure 4.3: Overflux computation.

As previously noted, the results concerning overfluxes exhibit consistency when considering lateral loading conditions applied along the x or y axes. Furthermore, it is evident that under identical longitudinal and lateral loading conditions with opposite signs, the overflux value remains constant. This phenomenon stems from the definition of overflux as outlined in Equation 4.4. Table 4.3 illustrates that all calculated overfluxes are negative. The most critical condition, highlighted in yellow, is observed during the aerodynamic phase as expected, owing to the combined effects of lift, drag, and gravity. Notably, the overfluxes consistently fall below the established threshold of 10% determined by the UM.
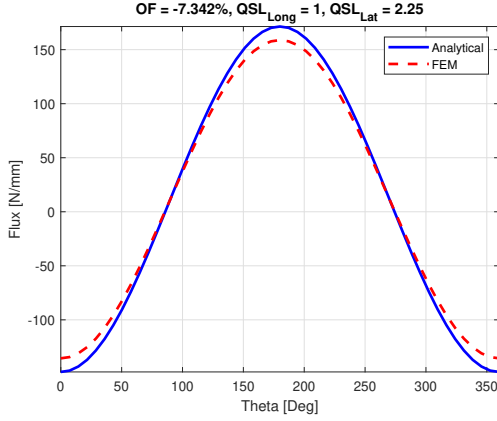
Figure 4.4: Overfluxes plot for $M_x = M_{Lat}$.
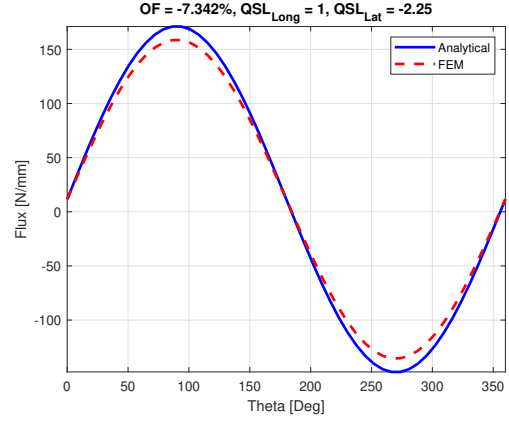
Figure 4.5: Overfluxes plot for $M_y = M_{Lat}$.

Figure 4.6: Analytical and FEM comparison

Figure 4.6 illustrates the behavior of both the aforementioned FEM and analytical model. It's important to emphasize the inherent disparity between the two computations: the analytical approach produces a continuous function that can be computed for the required values of theta and discretized accordingly, resulting in a dashed red curve. Conversely, the FEM analysis is deemed more realistic as it accommodates the asymmetries in the structure. However, FEM relies on the partitioning of the structure, including the adapter ring, resulting in an approximate piece-wise curve. To enhance the accuracy of the model and overflux computation, one potential solution is to decrease the element size, leading to a more refined mesh of the model under analysis. Although this entails a higher computational effort, it ensures a comprehensive analysis of the model.

4.4   Clamp band tension compliance
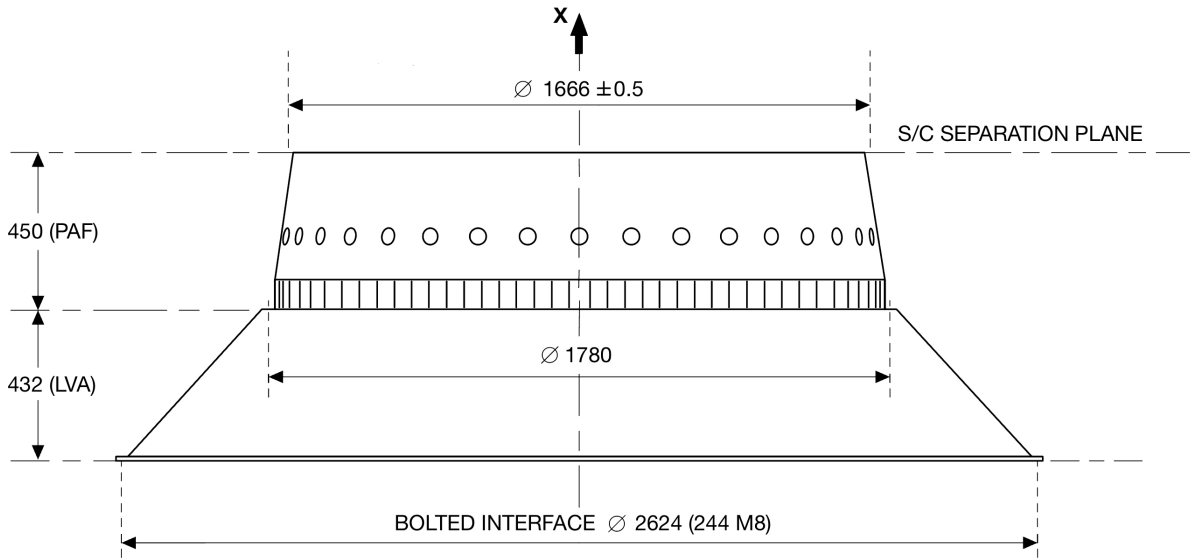
Figure 4.7: Spacecraft-Launcher Adapter.

Although compressive loading typically does not pose a critical concern for maintaining the SC and LV adapter attached via the clamp band, tensioning loading could lead to their separation. Hence, an appropriate clamp band tension is necessary to prevent the separation

of the SC. The commonly employed clamp system is the Marman clamp band, which securely holds together the two axial-symmetric parts of the interface using multiple V-shaped arch segments. These segments are pressed towards a tightening belt, and the clamp band tension is applied via a screw system. The tension is monitored using load cells distributed along the circumference as shown in Figure 4.7. The tightening force, directed through the V-shaped angle, applies a distributed compressive load between the two parts, effectively preventing their separation when subjected to tensioning loads:

$$T_{\min} = f_{\max}^{\mathrm{radial}} \, \mathrm{RIF} \, FOS \tag{4.5}$$

$$f_{\max}^{\mathrm{radial}} = 2 \cdot f_{\max} \cdot \frac{\tan(\alpha) - \mu}{1 + \mu \cdot \tan(\alpha)} \tag{4.6}$$

The Ring interface diameter (RIF) is a known parameter as defined as shown in Figure 4.7. μ represents the friction coefficient between the surface of the SC and the clamp, typically set at 0.1. The angle α corresponds to the V-shaped angle of the clamp, typically set at 15 degrees [1]. Initially set to 2 during the design phase, the Factor of safety (FOS) serves as a margin to address uncertainties, yet it remains subject to adjustment in more advanced design stages. The maximum tightening force is limited by the stresses sustainable by the interface ring parts. Here, $f_{\max}$ signifies the maximum tensional line load experienced during the mission, determined through previous static analysis and calculated using the analytical formulation, upon confirmation that the disparities between the analytic model and FEM fall within acceptable limits, as discussed in Section 4.3. Table 4.8 depicts the values of the actual tensional line load obtained with the introduction of the aforementioned friction coefficient μ.

| QSL_{Lat} [g]	QSL_{Long} [g]	$f_{\max}^{\mathrm{radial}}$ [N/mm]	QSL_{Lat} [g]	QSL_{Long} [g]	$f_{\max}^{\mathrm{radial}}$ [N/mm]
-7.5	1.25	55.5881	-7.5	1.25	55.5881
-7.5	-1.25	55.5884	-7.5	-1.25	55.5884
-4.5	2.25	65.2656	-4.5	2.25	65.2656
-4.5	-2.25	65.2658	-4.5	-2.25	65.2658
-4.375	-2.25	64.7906	-4.375	-2.25	64.7906
-4.375	2.25	64.7905	-4.375	2.25	64.7905
1	2.25	51.9641	1	2.25	51.9641
1	-2.25	51.9639	1	-2.25	51.9639
1.875	2.25	55.2894	1.875	2.25	55.2894
1.875	-2.25	55.2891	1.875	-2.25	55.2891
3.875	1.125	38.7980	3.875	1.125	38.7980
3.875	-1.125	38.8086	3.875	-1.125	38.8086

(a) $M_y = 0$, $M_x = M_{Lat}$ (b) $M_x = 0$, $M_y = M_{Lat}$

Figure 4.8: Maximum real line load.

The higher requirement arises from $f_{\max}^{\mathrm{radial}} = 65.2656\,\mathrm{N/mm}$, corresponding to a tightening force of $T_{\min} = 0.2\,\mathrm{MN}$. This result allows us to calculate the minimum tension targets for both cases of one or two tightening bolts, expressed respectively in Equations 4.7 and 4.8.

$$T_{\theta_1} = T_{\min} \cdot e^{\mu\pi} \tag{4.7}$$

$$T_{\theta_2} = T_{\min} \cdot e^{\frac{\mu\pi}{2}} \tag{4.8}$$

The minimum tension targets for both cases correspond to $T_{\theta_1} = 0.3\,\mathrm{MN}$ and $T_{\theta_2} = 0.2\,\mathrm{MN}$.

Chapter 5

LV-SC Dynamic Coupling Analysis

As seen on Chapter 3, one of the most vital requirements for a space mission is the one related to the fundamental frequencies of the Spacecraft. If not respected, there is a chance that the satellite and the Launch Vehicle resonate together, performing an harmonic coupled oscillation with increasing amplitude and associated accelerations. Eventually, the increasing loads are such that lead the mission to a catastrophic failure. In order to study such phenomenon, called Dynamic Coupling, an analysis on the effect of the Spacecraft's first natural longitudinal frequency over the response of the system Spacecraft-Launch Vehicle under harmonic excitation is performed.

5.1 3 DOF Large Mass Model

The selected model for the analysis is a simple 3 DOF one, that considers the Spacecraft and the Launch Vehicle as lumped masses, linked to each other by a spring and a damping elements (that represent the IF between them). Furthermore, the mass related to the Launch Vehicle is linked (also by a spring and a damping elements) to a Large Mass (much higher than the sum of the other two), to which an harmonic acceleration is imposed, hence the name of the model.
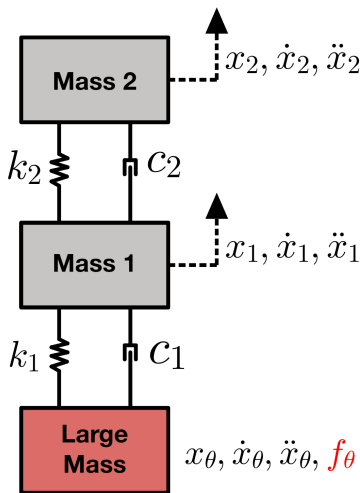

Figure 5.1: 3 DOF Large Mass Model.
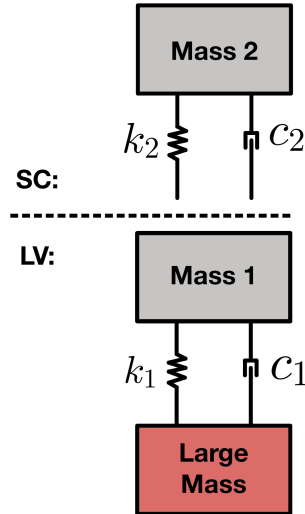
Figure 5.2: Spacecraft and Launch Vehicle's DOFs and parameters.

Figures 5.1 and 5.2 illustrate the model, where x, $\dot{x}$ and $\ddot{x}$ represent, respectively, the displacement, velocity and acceleration of each mass and the subscripts $()_1$, $()_2$ and $()_0$ refer

to the Launch Vehicle's, Spacecraft's and Large Mass' parameters. The frequency f_0 is the forcing term, that comes as an harmonic excitation applied to the Large Mass.

Table 5.1 contains the properties of each mass element of the model.

Parameter	Large Mass	Launch Vehicle	Spacecraft
Mass [kg]	$1 \cdot 10^{12}$	530000	6617.917
Fundamental Longitudinal Freq. [Hz]	-	17.64 (Free-free)	32.95 (Hard-Mounted)
Stiffness [N/m]	-	$6.5 \cdot 10^9$	$2.83 \cdot 10^8$
Damping [Ns/m]	-	$5.87 \cdot 10^6$	$1.37 \cdot 10^5$

Table 5.1: Lumped Mass elemets' parameters.

The stiffness and damping of the spring and damping elements were obtained based on the already known values of masses and longitudinal natural frequencies:

$$k = m \cdot (2\pi f) \tag{5.1}$$

$$c_{cr} = 2\sqrt{km} \tag{5.2}$$

$$c = c_{cr} \tag{5.3}$$

Where k, c_{cr}, c and f are the stiffness, critical damping, damping coefficient and Natural Frequency, respecting the defined subscripts. Furthermore, ξ represents the damping ratio, here assumed to be equal to 5% [2].

In mathematical terms, the system obeys to the following matricial system:

$$\begin{bmatrix} m_2 & 0 & 0 \\ 0 & m_1 & 0 \\ 0 & 0 & m_0 \end{bmatrix} \begin{pmatrix} \ddot{x}_2 \\ \ddot{x}_1 \\ \ddot{x}_0 \end{pmatrix} + \begin{bmatrix} c_2 & -c_2 & 0 \\ -c_2 & c_1 + c_2 & -c_1 \\ 0 & -c_1 & c_1 \end{bmatrix} \begin{pmatrix} \dot{x}_2 \\ \dot{x}_1 \\ \dot{x}_0 \end{pmatrix} + \begin{bmatrix} k_2 & -k_2 & 0 \\ -k_2 & k_1 + k_2 & -k_1 \\ 0 & -k_1 & k_1 \end{bmatrix} \begin{pmatrix} x_1 \\ x_2 \\ x_0 \end{pmatrix} = \begin{pmatrix} 0 \\ 0 \\ f_0 \end{pmatrix} \tag{5.4}$$

Representing in a compact indicial notation:

$$[m_{ii}] \left(\ddot{\boldsymbol{X_i}} \right) + [c_{ii}] \left(\dot{\boldsymbol{X_i}} \right) + [k_{ii}] \left(\boldsymbol{X_i} \right) = \left(\boldsymbol{F_i} \right) \tag{5.5}$$

Recalling the forcing term definition and assuming an harmonic solution as:

$$(x_i) = (\boldsymbol{X_i}) e^{j\omega t} \tag{5.6}$$

$$(f_i) = (\boldsymbol{F_i}) e^{j\omega t} \tag{5.7}$$

Where j is the imaginary unit, t is the time and ω is the angular frequency of the input. In the present case, the amplitude of the forcing term F is unitary. Note that $\boldsymbol{X_i}$ and $\boldsymbol{F_i}$ are complex vectors and have phases of their own.

By inserting the relations above into the compact system equation and assuming steady-state vibrations, one ends up with:

$$(-\omega^2 [m_{ii}] + \omega [c_{ii}] + [k_{ii}])(\boldsymbol{X_i}) = (\boldsymbol{F_i}) \tag{5.8}$$

Hence, the Frequency Response Function amplitude displacement and acceleration vectors may be obtained:

$$(\boldsymbol{X_i}) = (-\omega^2 [m_{ii}] + \omega [c_{ii}] + [k_{ii}])^{-1} (\boldsymbol{F_i}) \tag{5.9}$$

$$(\ddot{X}_i) = -\omega^2 (\boldsymbol{X_i}) \tag{5.10}$$

In this case, it is interesting to evaluate the behavior of the Spacecraft with respect to the base acceleration (which is the Large Mass one), so the Transmissibility, the ration between absolute amplitude acceleration values of the Spacecraft and Large Mass, is assessed:

$$T = \frac{|\ddot{x}_2|}{|\ddot{x}_0|} \tag{5.11}$$

This parameter's value reflects the coupling behavior between the mass elements of the system:

- **T=1**: The system behaves like a rigid body;

- $\boldsymbol{T < 1}$: The Spacecraft's acceleration is attenuated, presenting a smaller amplitude than the base's. This is the desirable case, with reduced loads acting upon the satellite;

- $\boldsymbol{T > 1}$: The Spacecraft's acceleration is amplified, presenting higher amplitudes than the base's and submitting the satellite to higher loads.

Finally, beyond the analysis of the Spacecraft-Launch Vehicle system, an additional case is studied, now considering the Large Mass as being the Launch Vehicle and the two lumped masses as the Spacecraft and the Telescope. The analysis follows the same terms as the original one, only this time considering the Telescope's parameters, presented in Table 5.2:

Parameter	Telescope
Mass [kg]	100
Fundamental Longitudinal Frequency [Hz]	90
Stiffness [N/m]	$3.2 \cdot 10^7$
Damping [Ns/m]	5652

Table 5.2: Telescope lumped mass parameters.

Where the Telescope's Longitudinal Fundamental Frequency was considered to be the same as the soft mounted one of the instrument used on ESA's mission CHEOPS (CHaracterising ExOPlanet Satellite) [3].

5.2   Results

5.2.1   Launch Vehicle - Spacecraft

Figure 5.3 contains the Transmissibility results with respect to the excitation frequency for various values for the Spacecraft's Fundamental Longitudinal Frequency. As it can be seen, as the fundamental frequency approaches the value of the Launch Vehicle's one, the maximum Transmissibility increases considerably. Such behavior was expected and reflects the effect of the dynamic coupling between Spacecraft and Launch Vehicle: considering the worst case scenario ($f_{SC} = f_{LV} = 17.64 \ Hz$), for a unitary acceleration input of 1g, the satellite would be submitted to a load of almost 50g.

Furthermore, if the longitudinal frequency has a value equal to the UM's requirement, the Transmissibility is reduced in 38.64% and decreases even further as far as its value gets from the Launch Vehicle's one. However, a caveat must be done with respect to the results: although they are useful to visualize the effect of dynamic coupling and help assessing it during preliminary phases of the design, due to the simple nature of the model, results cannot be taken as the numerically expected ones.

In order to provide a better visual insight on the effect of Dynamic Coupling, Figure 5.4 displays a 3D plot that represents how the Transmissibility changes according to the
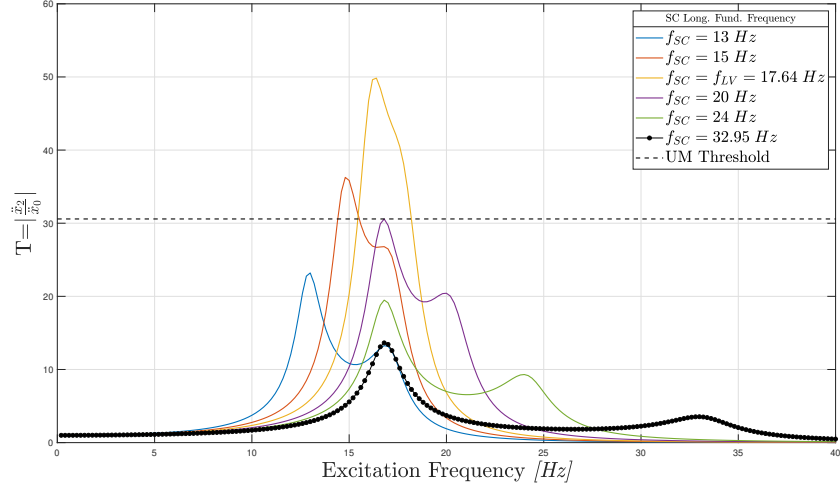
Figure 5.3: Transmissibility response at the Spacecraft for different values of the Longitudinal Natural Frequency.

Spacecraft's natural and the excitation frequencies. As anticipated, the highest found values are associated with both frequencies approaching the fundamental longitudinal frequency of the Launch Vehicle and decrease as they get farther from it.

Figure 5.4: Transmissibility resultant of an harmony excitation according to the Spacecraft's Longitudinal Natural Frequency.

Finally, Figure 5.5 shows the behavior of the maximum Transmissibility according to the chosen Spacecreft's fundamental frequency. For the actual Spacecraft's fundamental longitudinal mode $f_{SC} = 32.95 \ Hz$, highlighted as a red dot, it was found that $T_{max} = 13.64$, which is 72.63% less than the worst case scenario for $f_{SC} = f_{LV} = 17.64 \ Hz$. Moreover, in comparison with the UM's requirement, the reduction is of 55%.

It is important to notice that, as the natural frequency value distances itself from 17.64Hz, the observed reduction on the maximum Transmissibility is less effective. If, for example,

one increases the frequency from 20Hz to 30Hz (a rise in 50% in the value, half an octave), the resultant reduction is of 52%. On the other hand, if one goes from 30Hz to 45Hz (again rising the frequency in 50%), the Transmissibility decreases only by 20%.
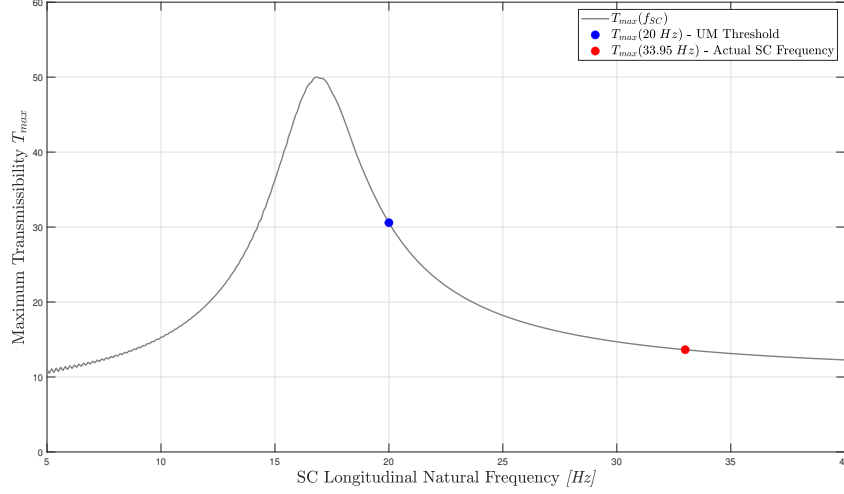
Figure 5.5: Maximum Transmissibility for each considered value of Longitudinal Natural Frequency.

5.2.2 Spacecraft - Telescope

A similar analysis was conducted, this time considering the dynamic coupling between the Spacecraft and the Telescope. As shown in Figures 5.6 and 5.7, results followed the same logic: for longitudinal natural frequencies of the Telescope closer to the value of the Spacecraft's one ($f_{TL} = 32.95~Hz$), a higher maximum Transmissibility is observed, while lower values happen for distant values.
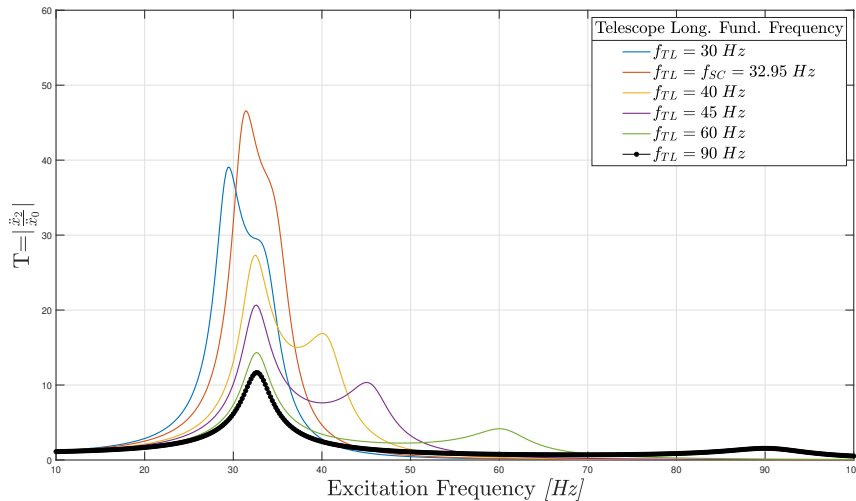
Figure 5.6: Transmissibility response at the Telescope for different values of the Longitudinal Natural Frequency.

In particular, the maximum response for the actual Telescope's fundamental longitudinal frequency ($f_{TL} = 90~Hz$, soft mounted) is $T_{max} = 11.66$. When compared with the correspondent value for the worst case scenario ($f_{TL} = f_{SC} = 32.95~Hz$), it represents a reduction

of 75%. Such result is expected, since the distance between both fundamental frequencies is around an octave and a half, hence, the dynamic coupling effect will be limited. A further reduction may be achieved by enhancing the stiffness of the top plate, where the Telescope is mounted.
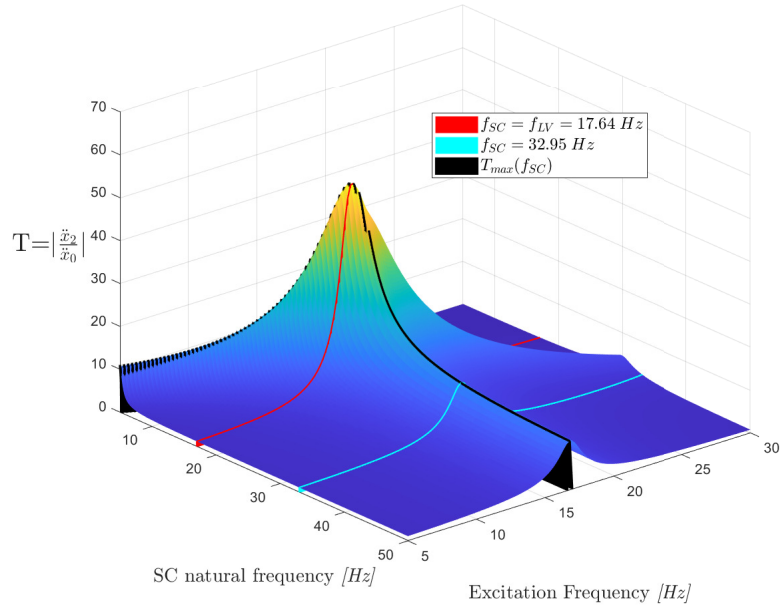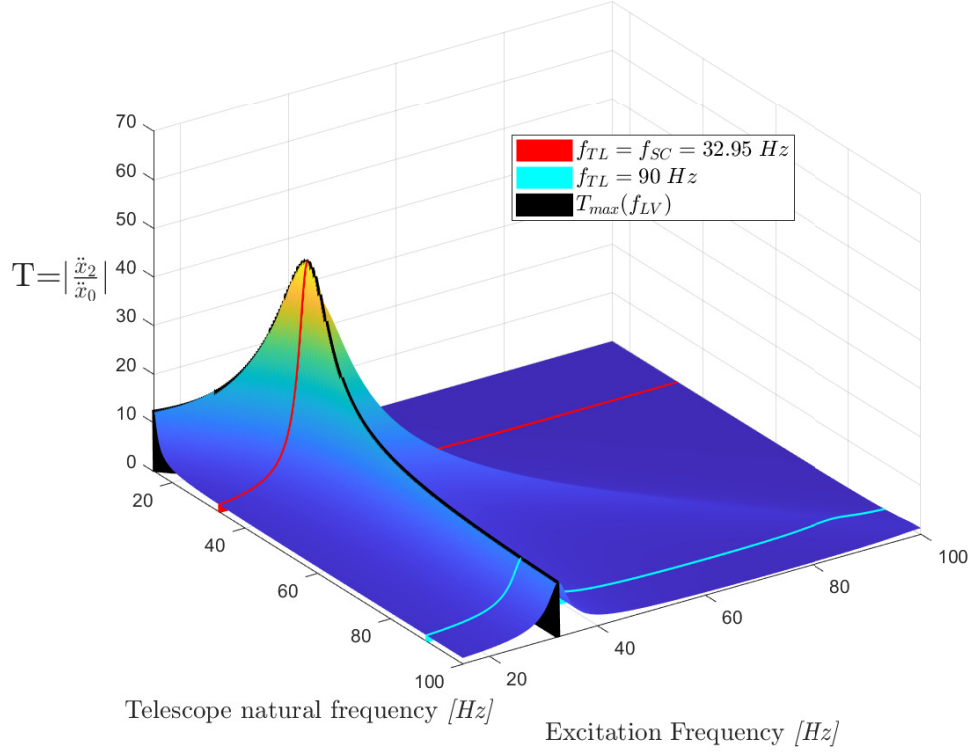

Figure 5.7: Transmissibility resultant of an harmony excitation according to the Telecospe's Longitudinal Natural Frequency.

Chapter 6

Thermoelastic analysis

6.1 Introduction

The thermal and structural design and analysis of space structures have garnered significant attention in recent years. Space structures typically comprise three-dimensional truss-type configurations, which are subjected to various forms of thermal loading, including solar radiation, infrared planetary radiation, and planetary albedo (solar radiation reflected from planets). It is crucial to determine the spatial and temporal variation of the temperature field within the structure resulting from these sources of radiation for effective thermal design. Moreover, the dynamic temperature field may induce dynamic deformation in the structure. Understanding this deformation is imperative due to constraints on the permissible deflection of instruments and antennas and the need to prevent resonance. In a specific scenario, the telescope mounted atop a spacecraft requires precise pointing toward a star, facilitated by onboard star trackers positioned on the structure's side. The objective is to analyze the spacecraft's pointing capability and quantify the relative rotations between the star tracker and the telescope under a thermal gradient. This analysis aims to identify thermoelastic biases, thereby enhancing overall pointing accuracy by accounting for this effect. It must be considered that an assumption has been made: in our ideal case, when thermoelastic effects are not taken into account, the bore-sights of the telescope and star tracker are aligned (this is not always true, for example if our telescope must point the Earth, the angle between bore-sights is typically 45 degrees, but this will over-complicate our analysis).The MSC Nastran solution is obtained through $template\_101\_Static-Thermoelastic\_run.dat$ sequence code for the linear static solution.

6.2 Thermoelastic model

In a more realistic design, the temperature values are given for an high number of nodes after an accurate thermal analysis, and then directly placed on the spacecraft surface. However, in this case the coordinates and temperatures of 60 points placed on the vertical edges of the parallelepiped enveloping the geometry of the structure are assumed, and the temperature of each surface node is defined by thermal interpolation. Assuming that one side of the spacecraft points to the sun, and the other side faces the deep space, half of the nodes are set to be at a temperature of $50°C$ and the other half is supposed to be at $-50°C$, as shown in Table 6.1. The temperature values are defined in this range because only the temperatures reached by the actual primary or secondary structure are considered. Therefore, the higher temperatures reached by the external Multi Layer Insulation (MLI) system are not taken into account, as they are not an integral part of the structure.

| $T = 50°C$ | | | $T = -50°C$ | | |
x	y	z	x	y	z
2	2	45.25	-2	2	45.25
2	2	45.66	-2	2	45.66
2	2	46.07	-2	2	46.07
2	2	46.48	-2	2	46.48
2	2	46.89	-2	2	46.89
2	2	47.30	-2	2	47.30
2	2	47.71	-2	2	47.71
2	2	48.13	-2	2	48.13
2	2	48.54	-2	2	48.54
2	2	48.95	-2	2	48.95
2	2	49.36	-2	2	49.36
2	2	49.77	-2	2	49.77
2	2	50.18	-2	2	50.18
2	-2	50.59	-2	2	50.59
2	-2	51	-2	2	51
2	-2	45.25	-2	-2	45.25
2	-2	45.66	-2	-2	45.66
2	-2	46.07	-2	-2	46.07
2	-2	46.48	-2	-2	46.48
2	-2	46.89	-2	-2	46.89
2	-2	47.30	-2	-2	47.30
2	-2	47.71	-2	-2	47.71
2	-2	48.13	-2	-2	48.13
2	-2	48.54	-2	-2	48.54
2	-2	48.95	-2	-2	48.95
2	-2	49.36	-2	-2	49.36
2	-2	49.77	-2	-2	49.77
2	-2	50.18	-2	-2	50.18
2	-2	50.59	-2	-2	50.59
2	-2	51	-2	-2	51

Figure 6.1: Parallelepiped temperatures.

To find the solution in MSC Nastran, the thermal properties of the material must be defined. In this case it has been considered for simplicity the Coefficient of Thermal Expansion (CTE) of the Aluminum ($\alpha_{Al} = 2.4 \cdot 10^{-5}$ $1/°C$) and the reference temperature has been imposed at $22.5°C$. These values are necessary to actuate the analysis, knowing that the law of thermoelastic effect is:

$$\Delta l = \alpha \cdot \Delta T \cdot l_0 \tag{6.1}$$

Where Δl is the deformation, $\alpha = \alpha_{Al}$, $\Delta T = T - T_{ref}$ and l_0 is the initial length.

For the thermal interpolation, each thermal node is set to influence only the 30% of the structure and the minimum number of locations to be included in the interpolation is set to 2.

Thermal map is defined in the Figure 6.2:
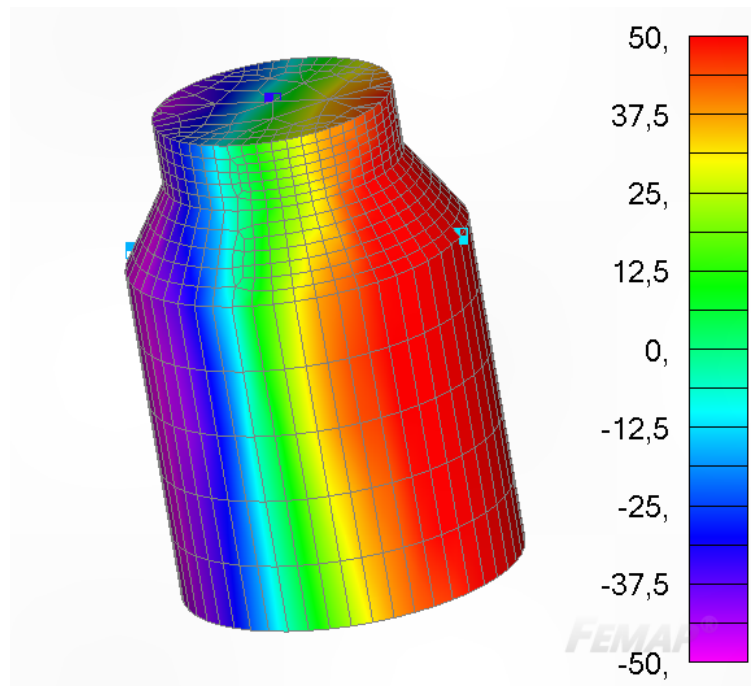
Figure 6.2: Thermal map [°C].

This thermodynamic analysis aims to representing the satellite in orbit, so there is no physical constrain on it. However if in the static analysis the constrain is missing, a singularity problem will arise, and the determinant of the stiffness matrix will be zero. In this case the analysis would not run.

To avoid this problem a constrain in a different form is given in the template of the 101 solution sequence code for the linear static solution: the MSC Nastran command PARAM, INREL, -2 exploits the inertia of the structure to constrain its CoG. This represents indeed the effect of a thermoelastic deformation in which the momentum is preserved.

6.3   Results
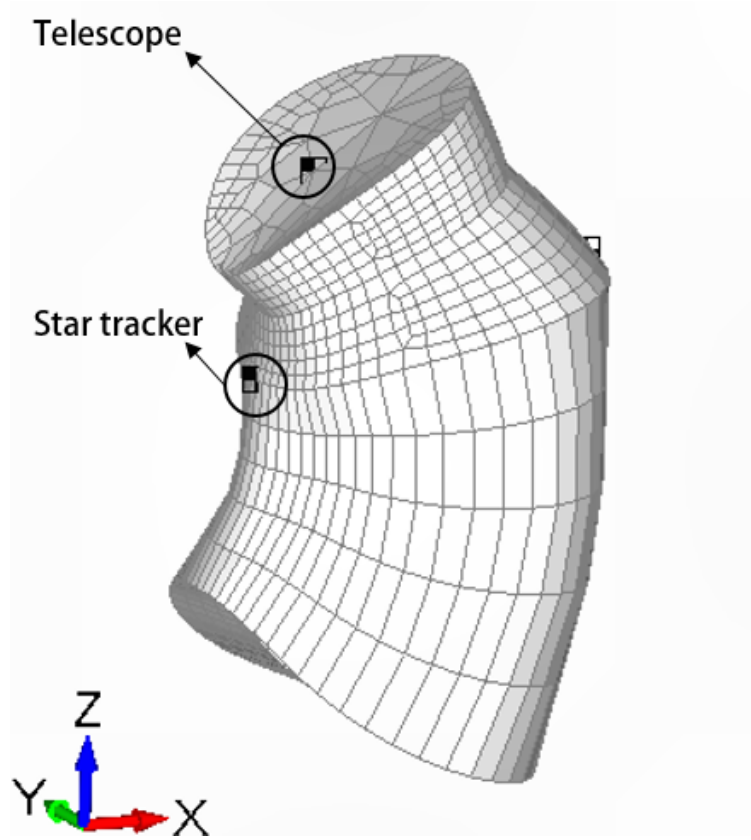
Figure 6.3: Thermoelastically deformed structure.

Unit	θ_x [deg]	θ_y [deg]	θ_z [deg]
Star Tracker	$-2.20 \cdot 10^{-6}$	$-2.16 \cdot 10^{-2}$	$-5.15 \cdot 10^{-6}$
Telescope	$-4.06 \cdot 10^{-5}$	$-1.52 \cdot 10^{-1}$	$3.53 \cdot 10^{-4}$

Table 6.1: Absolute rotations.

$|\theta_x^r|$ [deg]	$|\theta_y^r|$ [deg]	$|\theta_z^r|$ [deg]
$3.84 \cdot 10^{-5}$	$1.31 \cdot 10^{-1}$	$3.59 \cdot 10^{-4}$

Table 6.2: Relative rotations between star tracker and telescope.

As can be seen from Figure 6.3 and from Table 6.1, the spacecraft has a major rotation around the y-axis due to the thermoelastic effect. As consequence, in Table 6.2 can be noticed an high value in the relative rotations between spacecraft and telescope around this rotation.

This very high value of $|\theta_y^r|$ must be taken as a warning number, because this great value would not be acceptable for telescope pointing accuracy: even if this rotation is known, and could in theory be corrected a posteriori, any little error in the thermoelastic analysis could easily propagate to affect other quantities, thus affecting in any case the pointing performances of the SC.

Stating that this is only a preliminary design, in a real thermoelastic analysis the rotation values could be decreased through opportune design changes in the subsequent iterations. One possible methodology to solve this problem in the further phase steps is by decreasing

the material CTE (here assumed equal to the Aluminum one for simplicity), maybe using composite materials that have lower CTEs (they can be also negative in some cases) .

Proceding with the design iteration, also the stress field generated by the thermoelastic effect must be computed (here they are not calculated, due to the heavy output file that could be generated from MSC Nastran). In a real project this is a very important part that leads to the verification and validation of the structure margin of safety.

Chapter 7

Sine Test Prediction, Transient CLA and ESI Threshold

7.1   Introduction

The sine test during qualification testing phase has the main objective to assure that the Spacecraft will be able to sustain the low frequency transient loads present during the launch. Although the actual flight loads of such kind do not come in a sine form, since they are intrinsically transient, this harmonic function is able to replicate an equivalent effect.

This procedure is often indicated to be the severest moment in terms of mechanical loading of the Spacecraft's life cycle. Therefore, it is necessary to run computational simulations to predict the satellite's behavior when submitted to the excitement, in order to ensure the test's safety.

Here, the frequencies of interest range from 5 up to 100 Hz and are associated with an amplitude (expressed in gs), available at the Launcher's UM [1]. These values are used as the input profile performed by the shaker during the procedure, that is carried out exciting one Cartesian axis each time (in a total of three).

Sine	Frequency range (Hz)	Qualification levels (0-peak)	Protoflight levels (0-peak)	Acceptance levels (0-peak)
	2 - 5	12.4 mm	12.4 mm	9.9 mm
Longitudinal	5 - 50	1.25 g	1.25 g	1 g
	50 - 100	1 g	1 g	0.8 g
	2 - 5	9.9 mm	9.9 mm	8.0 mm
Lateral	5 - 50	1 g	1 g	0.8 g
	50 - 100	0.8 g	0.75 g	0.6 g
Sweep Rate		2 oct/min	4 oct/min	4 oct/min

Table 7.1: Ariane 6's sinusoidal vibration tests levels.

The evolution of the sine input evolves with time respecting a sweep function, continually increasing and covering all the desired frequency spectrum. Such equation takes the form of:

$$a_{sw}(t) = A(t) \sin\left(2\pi \frac{60 f_0}{K_e ln(2)} (2^{\frac{K_e}{60} t} - 1)\right) \tag{7.1}$$

Where K_e (expressed in oct/min) is the exponential sweep coefficient, value that dictates the pace with which the excitation frequency increases on time, f_0 is the initial frequency and $A(t)$ is the amplitude of the input.

In our case, both parameters are indicated on Ariane 6's UM, listed on Table 7.1, along with the test's frequency profile. However, an additional limit is also included for lower

frequencies: instead of the acceleration, the maximum stroke amplitude is given. This is justified by the fact that a same acceleration leads to higher displacements for these values:

$$\frac{A}{(f_0/2\pi)^2} = D_{stroke} \tag{7.2}$$

Hence, in order not to exceed the shaker's physical limitations, the maximum stroke is imposed.

7.1.1 Notching

Due to the test's harsh mechanical and conservative natures, some adjustments to the sine acceleration inputs are needed, with the objective to not overtest too much the structure and ensure the payload's safety during the procedure. Therefore, "Notchings" have to be imposed to the acceleration profile, that is, for certain frequencies the amplitude of the sine loading is reduced.

There are two kinds of Notchings, called primary and secondary, and their rationales are discussed below.

Primary Notching

The Primary Notching is mainly related to avoiding the mechanical overtesting of the structure and its motivation lies on the intrinsic differences between the Sine Tests, that use harmonic inputs, and the actual conditions the Spacecraft will be submitted to during launch, that are transient.

The practical consequence is that, during the test, the Item Under Test will start resonating as the shaker's input reaches its fundamental frequency, leading to a great increase on internal stresses and reaction forces at the interface with the moving table. Such behavior will much probably not occur during flight, due to the random and transient nature of the encountered loads.

Hence, a maximum ceiling value is imposed by monitoring the reaction forces acting at the connection between the satellite and the shaker. From the static analysis, it is possible to obtain the expected qualification IF Moments and Forces. The excitation spectrum is then notched so as to assure that the interface loads do not exceed such values.

Therefore, the Primary Notch is defined for each one of the three monoaxial analysis as described on Table 7.2:

Excitation Axis	Reference Load	Expression
Sine X	IF Moment Y	$M_y = K_Q \cdot a_{lat_{max}} \cdot m_{SC} \cdot CoG_z$
Sine Y	IF Moment X	$M_x = K_Q \cdot a_{lat_{max}} \cdot m_{SC} \cdot CoG_z$
Sine Z	IF Force Z	$F_z = K_Q \cdot a_{long_{max}} \cdot m_{SC}$

Table 7.2: Primary Notching definition for each monoaxial test.

Where, K_Q is the qualification factor (in general, 1.25), m_{SC} is the Spacecraft's mass, CoG_z is the Center of Gravity's Z coordinate, $a_{lat_{max}}$ and $a_{long_{max}}$ are the maximum lateral and longitudinal accelerations provided on the Launch Vehicle's UM.

In general, as anticipated before, the Primary Notching is applied for the frequencies associated to the satellite's natural modes, for which, as a result, an increase on the IF loads occurs.

Secondary Notching

The Secondary Notching, more straightforwardly, is the reduction on the excitation profile imposed to avoid the Payload's response from exceeding its maximum qualification accelera-

tion. Consequently, the dynamic loads sustained by the instrument during the procedure are monitored and the input is notched in order to keep them lower than the defined ceiling.

7.1.2   ESI

On the other hand, a minimum threshold must also be established, so that the test loads remain coherent with the magnitude of the ones faced during flight. Hence, this reference line should be adopted according to the actual launch transient loads, that can be retrieved through a Coupled Load Analysis, which considers the response of the Spacecraft attached to the Launch Vehicle's Upper Stage under a modal transient loading.

Such analysis considers a 1DOF model and gives as a result the Shock Response Spectrum, that is calculated by considering the maximum absolute value of the response for each frequency. In other words, this will be the acceleration's absolute value of the respective DOF, in this case, $\ddot{x}$:

$$SRS = max|\ddot{x}(t, f)| \tag{7.3}$$

The Shock Response Spectrum (SRS) of the assembly should then be converted into an Equivalent Sine Input, that is an equivalent excitement profile (with same amplitude) the shaker must replicate to recreate the launch transient loads. This is done by dividing the SRS result by a qualification factor Q (not to be confused with K_Q), defined as the inverse of two times the interface's damping:

$$Q = \frac{1}{2\zeta} \tag{7.4}$$

Finally, one may obtain the ESI:

$$ESI = \frac{SRS}{Q} \tag{7.5}$$

The ESI line is then used as a reference: whenever the test excitement profile has values below it, the conditions of the procedure are considered to be lower than the ones required for qualification purposes.

7.2   Femap model and Simulation Setup

Based on the information presented throughout the last sections, in order to perform the Sine Test Prediction analysis, two types of analysis have to be performed: one in which the Spacecraft's FE model is excited monoaxially with sine-shaped loading and another modal transient one that uses a model accounting also for Ariane 6's Upper Stage, without fairings, as to replicate the results of a CLA and find the ESI curve.

7.2.1   Sine Test Prediction

The same FE model of the Spacecraft used on previous analysis (constructed using Femap) is considered here, with the only addition of two nodes, that represent the moving table and its interface with the Spacecraft.

One of them, is connected directly to the IF ring nodes, performing a *master-slaves* relation. In other words, the created node has an independent motion (dictated by the sinusoidal excitation input profile) that controls the motion of its *slaves*. The connection between these nodes is made via infinitely stiff elements of the RBE2 type.

On the other hand, the other node is the one that receives the input load directly and is connected to the master node by six highly stiff spring elements of the CELAS2 type, that mediate the transmission of the input. Hence, it is possible to recover the IF moments and forces.

Figures 7.1 and 7.2 show, respectively, the FE model and, in detail, the nodes and elements representing the effect of the moving table and its interface with the Spacecraft.
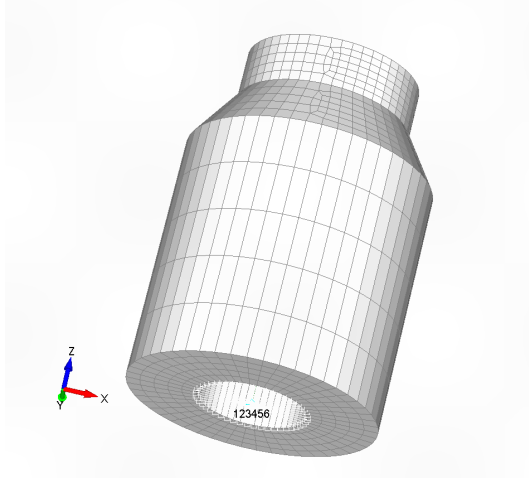
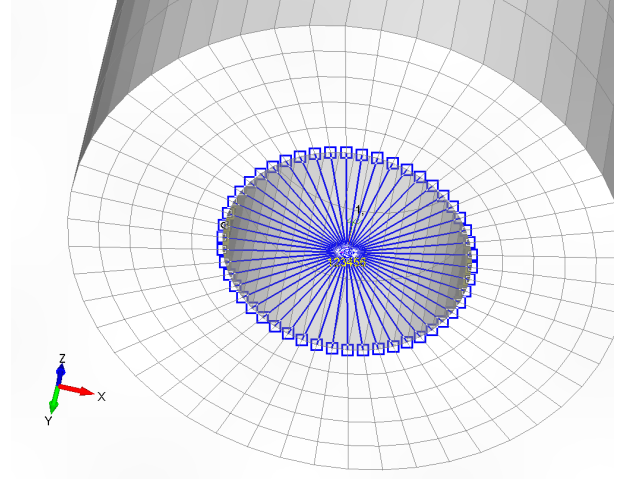Figure 7.1: Spacecraft's FE model used on the Sine Prediction analysis.

Figure 7.2: Detail of the FE model.

With the developed model, for each axis, a sine 1g excitation simulation was performed utilizing the MSC Nastran solver (*template_111_sine.dat*), having as outputs the desired IF Loads and accelerations respective to the node where the Payload is positioned. Later on, due to the method's linear elastic nature, these results will be scaled based on the excitement input profile provided in the Launch Vehicle's UM.

7.2.2 Transient CLA

The CLA is associated with a combined response to a transient loading and, therefore, considers both the Spacecraft and the Launch Vehicle. For the purpose of complying with the analysis' objectives, a FE model that contains the Spacecraft attached to Ariane 6's Upper Stage (without the fairings) was created on Femap. As in the Sine Prediction case, two nodes were created, but, this time, they are positioned inside the Upper Stage's nozzle.

Figures 7.3 and 7.4 show, respectively, the created FE model and the IF nodes and elements, in detail.
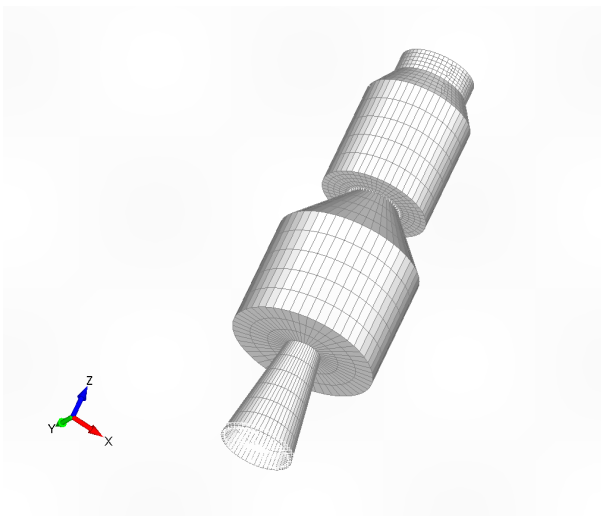

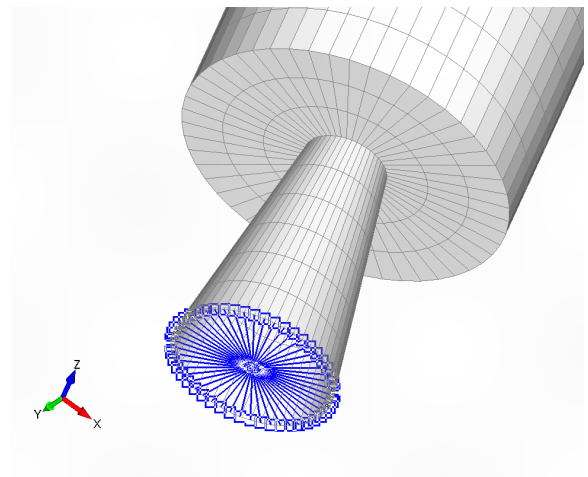Figure 7.3: Spacecraft and Ariane 6's Upper Stage FE model used on the Modal Transient analysis.

Figure 7.4: Detail of the FE model.

In order to obtain the ESI, first the createdFE model was submitted to a transient modal

analysis ($Template\_112\_Modal\_Transient.dat$), considering monoaxial transient loads illustrated on Figure 7.5. Then, the obtained response of the Spacecraft's IF node was used as an input to the $From\_SRS\_to\_ESI.xlsm$ Excel Spreadsheet. This spreadsheet calculated, through an iterative process, the equivalent SRS, which was then divided by the given qualification factor Q to obtain the ESI.
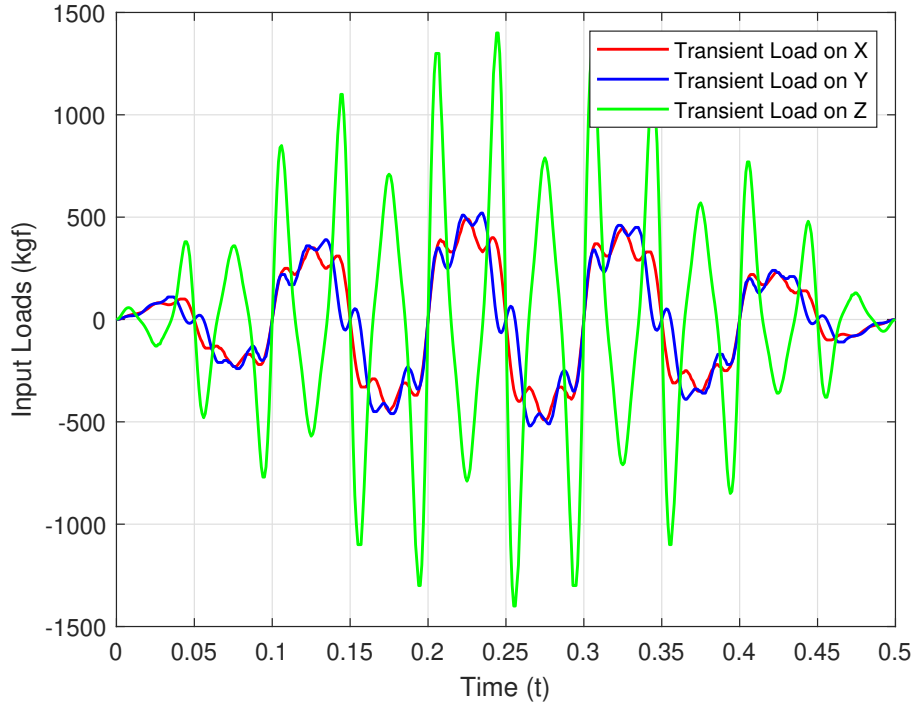

Figure 7.5: Transient loading profile used as an input of the Modal Transient analysis.

7.3 Analysis Specifications

7.3.1 Excitation Profile

Table 7.3 contains the sinusoidal excitation profile equivalent to the expected low frequency launch transient loads, as indicated by Ariane 6's UM [1]. These values will be, later on, notched according to maximum values for IF Lateral Moments and Longitudinal Force, as well as to the Payload's qualification level.

Direction	Frequency band (Hz)	Sine Amplitude (g)
Longitudinal	2 - 50	1.0
	50 - 100	0.8
Lateral	2 - 25	0.8
	25 - 100	0.6

Table 7.3: Ariane 6's sine excitation at spacecraft base.

Along with the results of the 1g loading cases, it is possible to obtain the desired results only by scaling the values acquired, simply multiplying then by the respective acceleration of the notched excitation profile.

7.3.2 Primary Notching

Considering the maximum lateral and longitudinal QSLs contained on Table 4.1 and a qualification factor of $K_Q = 1.25$ (system level), Table 7.4 contains the ceiling values for the IF lateral moments and longitudinal force considered for the Primary Notching analysis.

M_y[kgf m]	M_x[kgf m]	F_z[kgf]
40542.6622	40542.6622	49635

Table 7.4: Ceiling values for Primary Notching.

7.3.3 Secondary Notching

Here, standard values for the qualification levels of the Payload are adopted. Table 7.5 shows the maximum accelerations for the lateral and longitudinal cases.

Lateral Qualification Level (g)	Longitudinal Qualification Level (g)
15	20

Table 7.5: Qualification levels for the adopted Payload.

7.3.4 ESI

For the ESI's computation, a damping of $\zeta = 2\%$ is considered, hence $Q = \frac{1}{2\zeta} = 25$.

7.4 Results

7.4.1 Excitation on X

Considering the excitation on X, it is possible to note that, without the primary notching, the profile indicated by the Launch Vehicle's UM would result in IF Lateral Moments values that exceed the qualification one (as shown on Figure 7.7), as well as accelerations that are above the Payload's mechanical specifications (as seen on Figure 7.6).
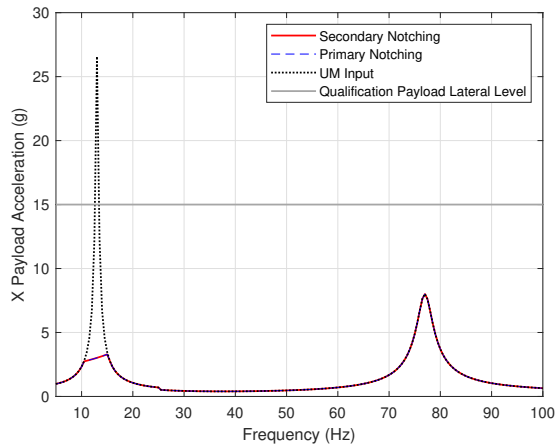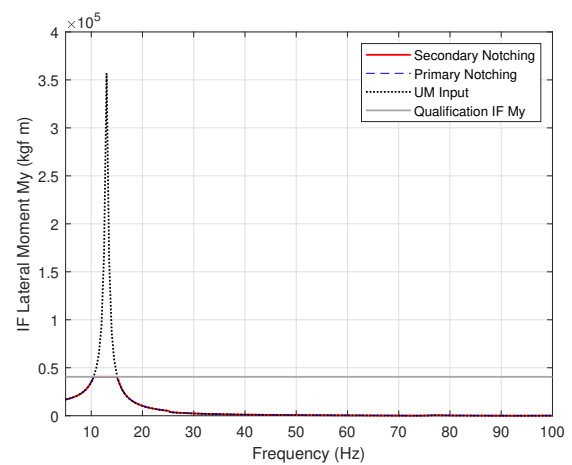

Figure 7.6: Payload's acceleration along X axis.

Figure 7.7: IF Lateral Moment around Y.

In this case, the primary notching was sufficient to reduce both levels of moment and acceleration below the ceiling values, that would happen on the surroundings of the Spacecraft's first lateral fundamental frequency (13.01 Hz, Hard-Mounted). Hence, no secondary notching was imposed.

Furthermore, as it can be seen from Figure 7.8, the reduction caused by the primary notching did not lead to a violation of the ESI and the resultant Test Input Profile was maintained above this threshold.
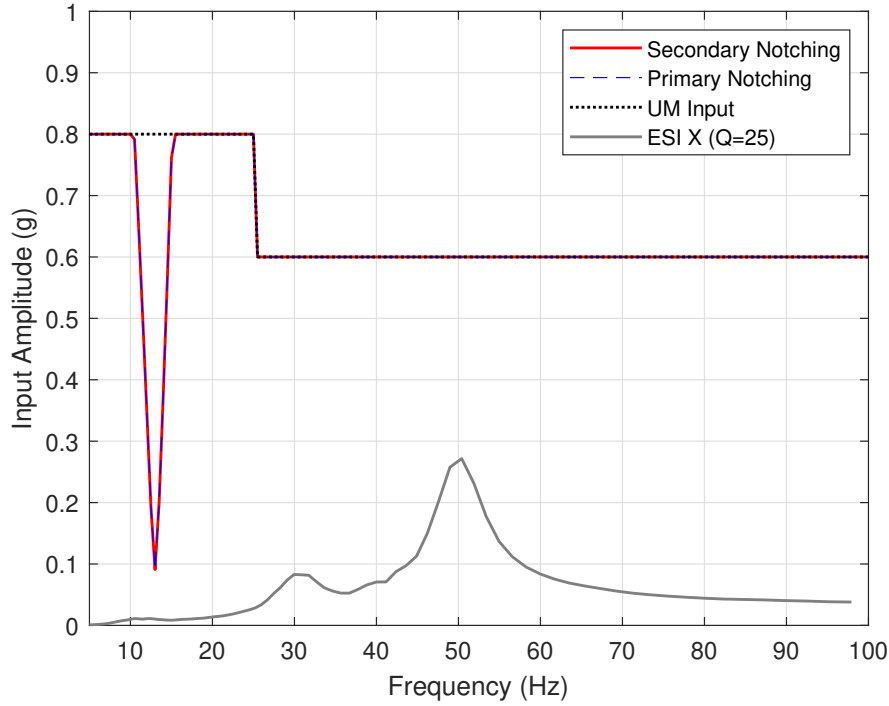

Figure 7.8: Input Profiles for sine excitation on X axis.

7.4.2 Excitation on Y

Regarding the analysis of the monoaxial excitation on the Y axis, considerably close results were obtained, when compared to the previous case, which is justified by the model's symmetry, besides from the two mass elements that are positioned aligned with the Y direction. Therefore, same responses were observed and, again, only a primary notching around the fundamental lateral frequency was imposed. Figures 7.9 and 7.10 contain, respectively, the Payload's acceleration and the IF Lateral Moment profiles before and after notching.

Nevertheless, as it can be seen from Figure 7.11, the ESI line was different from the X axis case. This might be related to the considered loads for the CLA, as shown on Figure 7.5, that were different for the two axes, associated with the already cited mass asymmetry. Even so, such limit was not crossed and the resultant profile was compliant with this requirement.
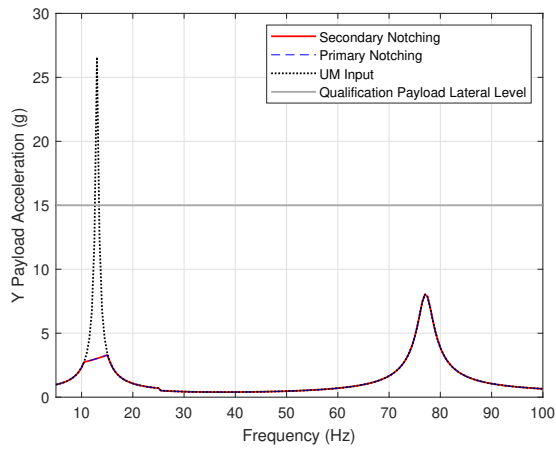
Figure 7.9: Payload's acceleration along Y axis.
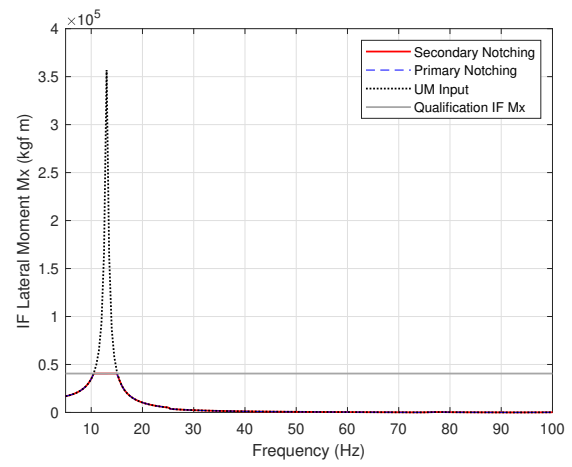
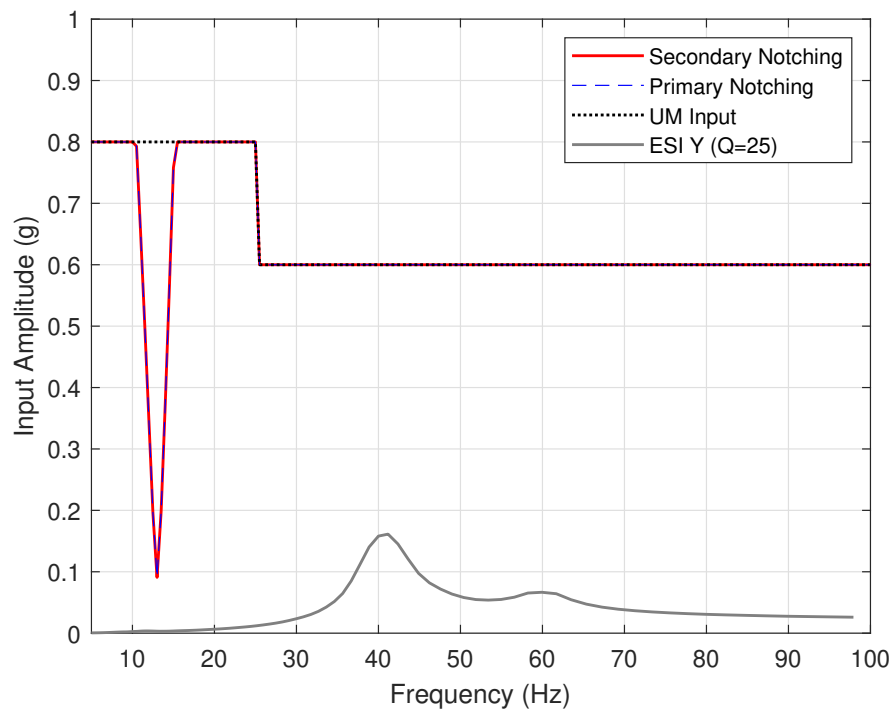Figure 7.10: IF Lateral Moment around X.

Figure 7.11: Input Profiles for sine excitation on Y axis.

7.4.3 Excitation on Z

Finally, for the longitudinal sine excitation the response to the unotched profile also achieved higher values than the settled limits in terms of IF Longitudinal Forces (Figure 7.13) and Payload acceleration (Figure 7.12).

Moreover, once more, it was necessary to impose a primary notching for the amplitudes associated with the fundamental longitudinal frequency (32.95 Hz). And, again, this was sufficient to also conform the profile to the requirements related to the Payload's Qualification Level.
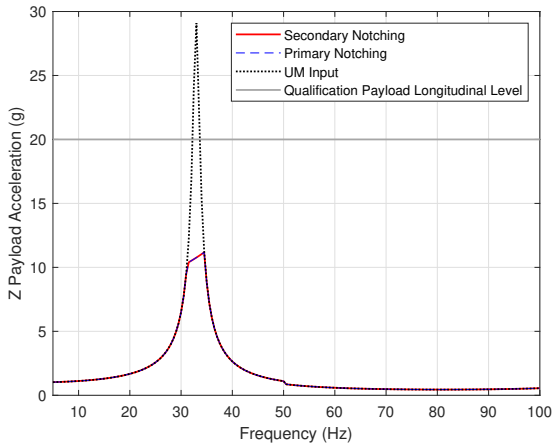

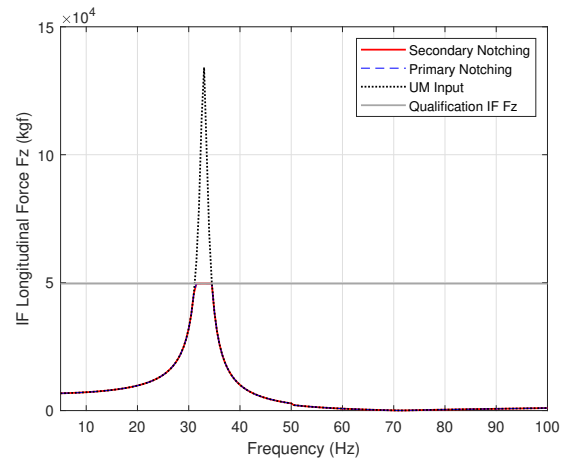Figure 7.12: Payload's acceleration along Z axis.

Figure 7.13: IF Longitudinal Force.

Figure 7.14 illustrates the resultant test profile that, even after notching, remains above the ESI line.
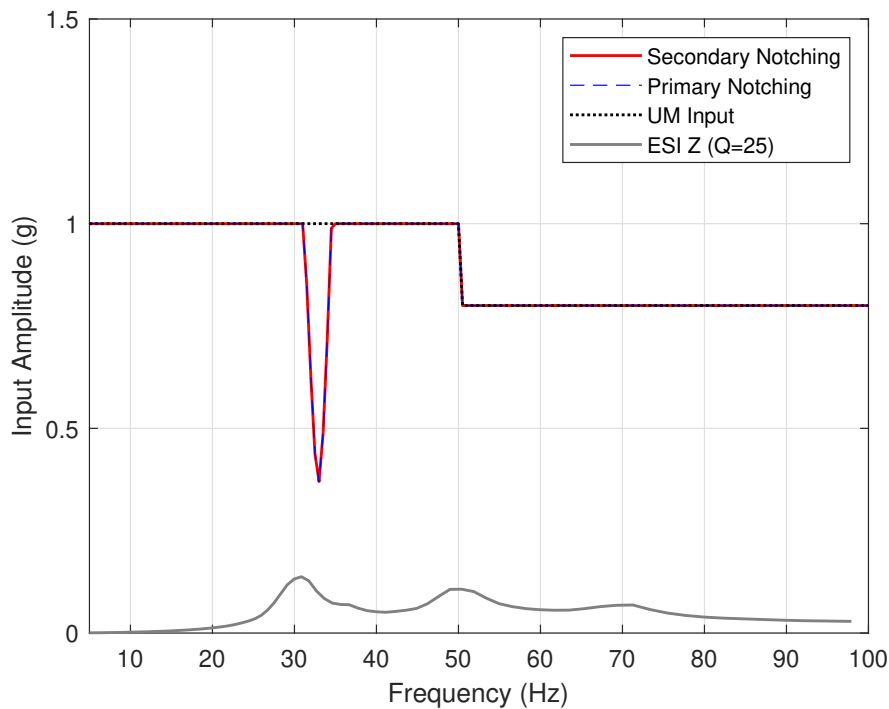

Figure 7.14: Input Profiles for sine excitation on Z axis.

Chapter 8

Acoustic analysis

8.1 Input analysis and process

This analysis retrieves the behaviour of SC telescope in terms of acceleration when it is subjected to acoustic pressure loads through *template_111_Modal_Random_SC_Acoustic.dat*. To run the analysis on MSC Nastran Sound Pressure Levels (SPL) must be achieved from [1]. The Pressure Root Mean Square (P_{RMS}) is computed using the human audibility lower threshold as Pressure reference (P_{ref}): $P_{RMS}^2 = P_{ref}^2 10^{\frac{SPL}{10}}$. So Pressure Power Spectral Density (PPSD) is taken by exploiting the bandwidth Δf_c of each relative frequency of the octave center f_c. So, PPSD is divided by the gravity acceleration in order to obtain an output Acceleration Power Spectral Density (APSD) in g^2/Hz. Finally, OverAll Sound Pressure Level (OASPL) is given by: $OASPL = 10\log(\sum_{i=1}^{710} 10^{\frac{SPL_i}{10}})$. These quantities are reported in the Table 8.1.

$f_c[Hz]$	$SPL[dB]$	$P_{RMS}^2[Pa^2]$	$PPSD_{\Delta f_c}[Pa^2/Hz]$	$PPSD_{\Delta f_c}[g^2Pa^2/Hz]$
31.5	128	2523.8	113.31	1.177
63	131	5035.7	113.04	1.175
125	136	15924.3	180.16	1.872
250	133	7981	45.15	0.469
500	129	3177.3	8.99	0.093
1000	123	798.1	1.13	0.012
2000	116	159.2	0.11	0.001
OASPL [dB]	139.5			

Table 8.1: The Pressure Power Spectral Density computation.

8.2 Simulation and qualification level

Unitary pressure loading have been applied to each plate element and re-scaled according to the equivalent pressures obtained. The SC is tested by applying these pressure loads on external and internal elements in order to be conservative. The elements will vibrate, making the components vibrate themselves. The analysis has been conducted within the frequency range 20-2000 Hz because higher frequencies require high cpu memory and 2000 Hz is already a conservative value. Infact, majority of the energy that makes the satellite vibrate is below this value.

An equipment mass major than 50 kg has been considered, since Ariane VI can bring to space heavy payloads and telescope mass can reach the order of hundreds of kg. This bring to have lower loads because the higher the mass the higher the endurance to excitation.

In addiction, being Ariane VI a european launcher, European Cooperation for Space Standardization (ECSS) qualification level in Table 8.2 has been used ([2]). The resulting mean acceleration of the random profile is 11.14 Root Mean Square acceleration (gRMS), where $gRMS = \sqrt{\sum_{i=1}^{7} \int_{f_i}^{f_{i+1}} APSD_i df}$.

For this case the qualification level is the same both for perpendicular mounting plane (out-of-plane direction) and for parallel mounting plane (in-plane direction).

Frequency range [Hz]	Qualification level
20-110	$+3 \ dB/oct$
110-700	$0.09 \ g^2/Hz$
700-2000	$-3 \ dB/oct$

Table 8.2: ECSS qualification level.

8.3   Results

Nastran pch file sets the acceleration outputs as a function of a range of frequencies in series 3,4,5 corresponding to the x,y,z direction of the acceleration of the node to which the mass of telescope is concentrated. As expected, the out-of-plane direction is the most critical because it approaches the threshold that unit can sustain. However, the qualification level is not crossed, so the unit is qualified to survive at accelerations of acoustic environment. As a consequence, the telescope can be designed in the modelled position.

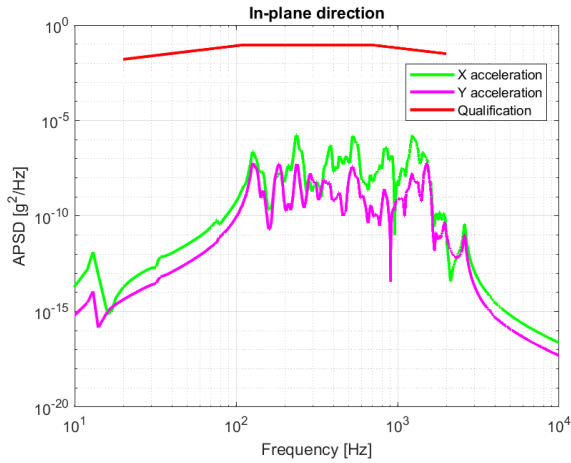Outcomes of test prediction analysis can be appreciated in the Figure 8.1 and 8.2.

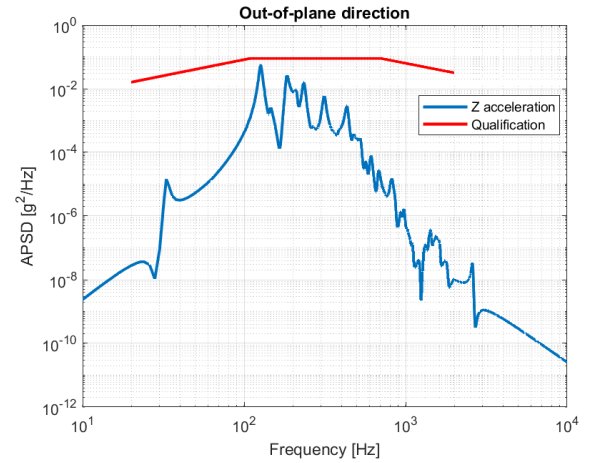Figure 8.1: Acoustic test for in-plane direction.

Figure 8.2: Acoustic test for out-of-plane direction.

Chapter 9

Severity Comparison

9.1   Introduction

This analysis is aimed to compare the severity associated with different load qualification tests. The focus of this comparison is on the sine test, random test, shock test, and the predicted acoustic test in order to identify the most critical load for each excitation frequency. The analysis considers a mechanical dynamic IF load expressed in terms of acceleration or APSD. The IF load severity associated to a certain frequency f is defined as the maximal acceleration experienced by a 1 DOF system with a natural frequency equal to the excitation frequency (f), subjected to the loading acceleration at its base [2].

The rationale behind severity comparison lies in the assumption that if a structure (real Multiple Degree of Freedom (MDOF) system) survives a certain severity of an IF load, it will likely survive another load, even if of a different nature, with the same severity. It is crucial to note that this analysis only accounts for failure from stress, neglecting fatigue-related issues, which are typically not significant for space structures due to their limited number of cycles, except for specific dynamical components like gyroscopes or inertial sensors.

9.2   Methodology

The mechanical load severity is computed according to the nature of the load qualification test:

- **Sine environment**: the severity g-spectrum is approximated by the SRS of the sine amplitude acceleration A(f):

$$SEV(f)_{sine} \approx A(f) \cdot Q$$

  where Q is the quality factor. In order to have a good approximation, sine profile and sine sweep rate should be low.

- **Random environment**: the severity g-spectrum of a qualification random APSD profile is given by the Extreme Response Spectrum (ERS) of it:

$$SEV(f)_{random} = ERS(f)$$

- **Shock environment**: the severity g-spectrum of a qualification shock profile is self-evident since a shock profile is already obtained as the SRS(f) of a time-history:

$$SEV(f)_{shock} = SRS(f)$$

Since a single severity level by itself does not provide any information concerning the maximum acceleration reached by the Item Under Test (IUT), the severity levels have to be compared among each others. In order to perform a consistent evaluation, the three severity levels aforementioned are conventionally retrieved by setting the quality factor $Q = 10$.

9.3 Results

By conducting different qualification tests, the global severity profile can be retrieved. Specifically, sine qualification test is more severe at low frequencies ($5Hz \div 110Hz$), random qualification test is more severe at middle frequencies ($20Hz \div 2000Hz$) while shock qualification test is more severe at high frequencies (up to $10000Hz$).

Qualification	Frequency Band [Hz]	Qualification Levels	
		Out of Plane	In Plane
Sine	5 - 21	11 mm	11 mm
	21 - 100	20 g	20 g
Shock	100	100 g	100 g
	2000 - 10000	2000 g	2000 g

Table 9.1: Sine and Shock tests inputs.

In Table 9.1 the qualification sine and shock levels are reported, in accordance with [2]. The random qualification level is still considered, as it is defined in Section 8.2.
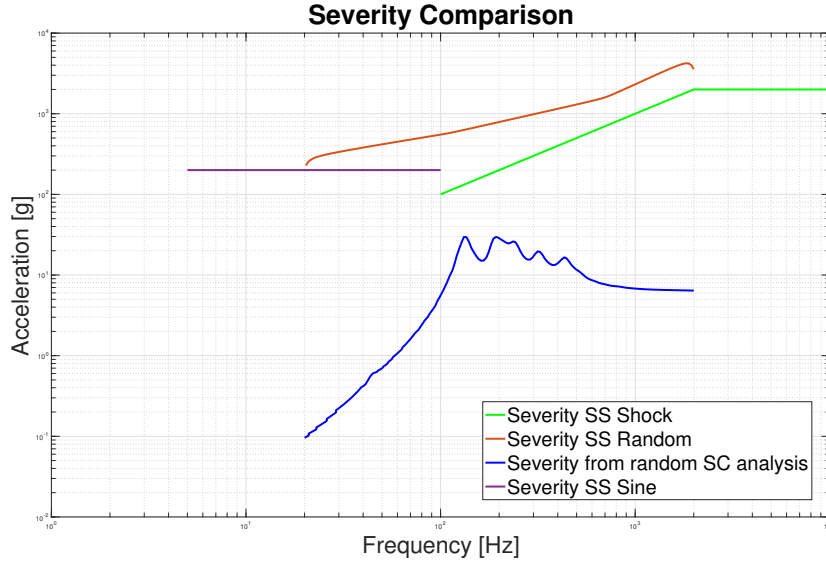

Figure 9.1: Severity Comparison.

From this comparison is evident that the severity curve associated with the test predictions conducted on the SC model consistently falls below the qualification thresholds. As a result, the telescope unit meets the qualification criteria not only for the entire frequency range of 20 to 2000 Hz but also up to 10000 Hz. This is supported by the fact that the APSD peaks obtained from the acoustic test predictions do not exceed the specified random qualification levels. Moreover, there is no anticipation of additional peaks at the highest excitation frequencies, as it can be seen in Figure 8.1 and 8.2.

9.4 Remarks

The severity comparison across different load tests is a valuable approach for identifying critical loads and ensuring the structural integrity of space systems. By understanding the severity associated with each excitation frequency, engineers can optimize designs and qualifications to enhance the reliability of space structures. The analysis provides insights into potential vulnerabilities and aids in the development of robust systems capable of withstanding a range of dynamic environments.

Chapter 10

Buckling Analysis

10.1   Introduction

In the ambit of structural analysis and design, engineers typically focus on ensuring the adequacy of structures under the strength and stiffness criteria. The first one guarantee that the stresses induced by specific loading scenarios remain within an allowable range, the latter establish constraints on deflections, strains and in some cases natural frequencies. What is missing from these two analysis is a characterization of the stability of our structure, which could be responsible for an early failure.

Buckling is one way a structure can fail under compression of a relatively thin structural component (much longer than wide). It causes a sudden alteration in the shape of the structure, leading to its collapse.

For these reasons the SC FE model has been subjected to a Buckling analysis

10.2   Finite Element Analysis

The analysis carried out by the team is composed of two parts: pre-buckling analysis and buckling analysis.

10.2.1   Pre-buckling analysis

This analysis involves constraining our structure at the IF ring and applying a set of external loads given by the QSL found in the LV UM, multiplied by a SF of 1.25 [1]. The results of this preliminary analysis provide us with the displacements, constraint forces, and internal loads of the structure. Regarding longitudinal loads, only the compressive ones were considered. For lateral loads, we examined both the +X and +Y directions. This choice stems from a slight asymmetry in the SC due to the positioning of the star trackers along the X-axis. Although the mass of these instruments is minimal and thus has little to no impact, conducting the lateral analysis on both axes allows us to identify the most critical scenario and ensures completeness.

10.2.2   Buckling analysis

The second step is carrying out the actual buckling analysis, which entails an eigenvalue problem that yields a set of eigenvalues; these are the factors by which the loads must be multiplied to reach buckling; of course the critical one is the minimum eigenvalue, which makes possible to define the following Margin of Safety (MoS).

$$\text{MoS} = \lambda_{\min} - 1 \tag{10.1}$$

10.3   Results

In this section are discussed the results obtained by the Nastran analysis after computing the numerical solution for the linear Buckling ("SOL 105").

In table Table 10.1 are reported the minimum eigenvalues for each load scenario:

Load from critical flight events	Longitudinal Load [g]	Lateral Load (along +X) [g]	$\lambda_{\min}$
Lift-Off	-4.375	2.25	407.38
Aerodynamic phase	-4.5	2.25	404.07
Pressure oscillations	-7.5	1	359.51
ESR jettisoning	-5	1.125	527.27
LLPM	-5.375	0.625	503.00
ULPM	-5.625	3	481.00

Table 10.1: Results of buckling analysis (lateral load along +X).

Load from critical flight events	Longitudinal Load [g]	Lateral Load (Along +Y) [g]	$\lambda_{\min}$
Lift-Off	-4.375	2.25	407.38
Aerodynamic phase	-4.5	2.25	404.07
Pressure oscillations	-7.5	1	359.51
ESR jettisoning	-5	1.125	527.27
LLPM	-5.375	0.625	503.01
ULPM	-5.625	3	481.01

Table 10.2: Results of buckling analysis (lateral load along +Y).

From these results it stands out that from a buckling point of view the structure is very conservative. The most critical load is the one given by pressure oscillations, for which we find a MoS of respectively 358.51, so the pressure oscillations QSL would have to be more than three hundreds times its value in order to induce buckling.

In Figure 10.3 and Figure 10.2 are reported the results displayed in Femap after the analysis.
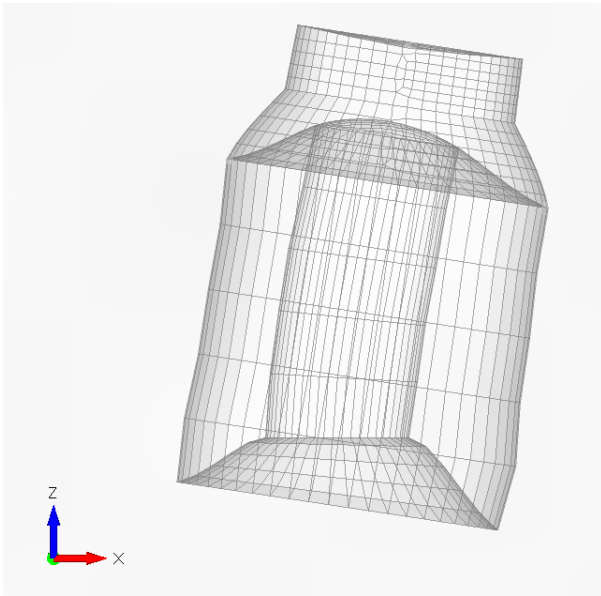
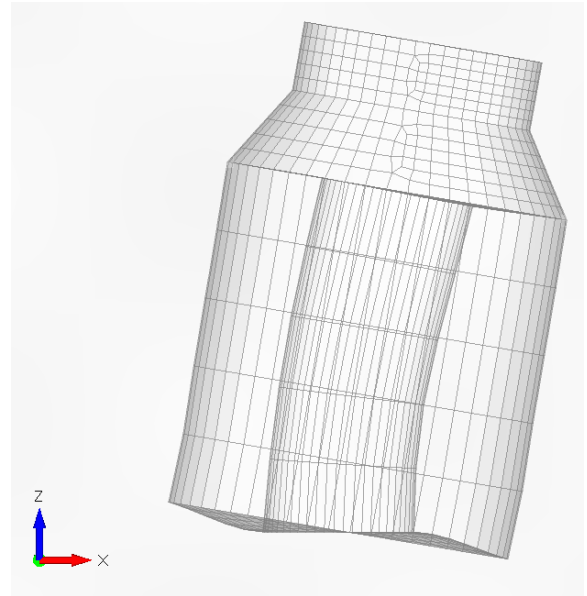Figure 10.1: Pre-buckling deformation (deformation scale: 10).

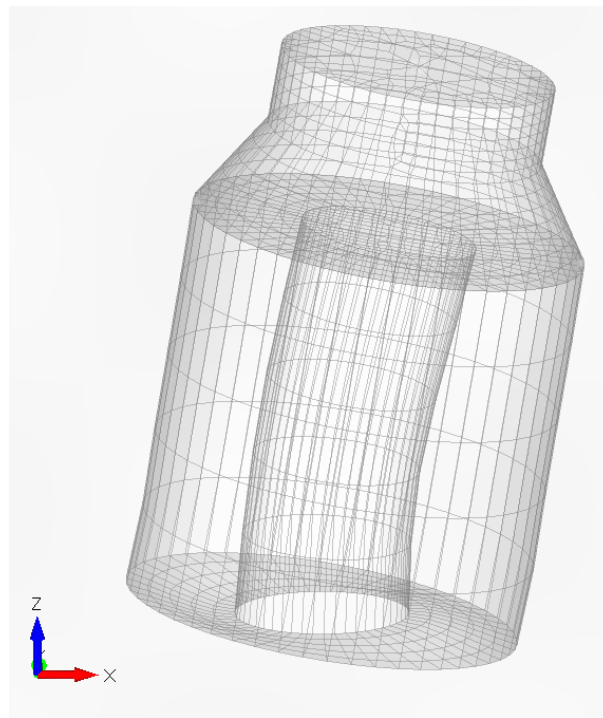Figure 10.2: Buckling mode shape associated to $\lambda_{\min}$.

Figure 10.3: Another view of the first buckling mode shape.

Chapter 11

Compliance summary

In Table 11.1, all subparts analyzed during this project are listed. When the test yields favorable results, it is labeled as compliant; conversely, when the results are unfavorable, it is labeled as non-compliant.

Analysis	Compliant/not compliant	Notes
Usable volume	Compliant	None
Mass and CoG	Compliant	None
Lateral frequency	Compliant	None
Longitudinal frequency	Compliant	None
Line loads	Compliant	None
Thermoelastic	Completed Criticality found	Relative rotations telescope- -star tracker too high
Sinusoidal Vibration test	Compliant	None
Acoustic	Compliant	None
Buckiling	Compliant*	Results are very conservative

Table 11.1: Compliance summary.

Bibliography

[1]   Ariane. *ARIANE 6 USER'S MANUAL*. Ariane, 2018.

[2]   Pietro Nali. "Analysis and Testing course". 2023-2024.

[3]   Willy Benz. "CHaracterising ExOPlanet Satellite - Definition Study Report". In: (2013).